Eindhoven University of Technology

MASTER

Helium transport and exhaust measurements with an ITER-relevant spectroscopic technique

Boom, J.E.

Award date:
2007

Link to publication

Disclaimer
This document contains a student thesis (bachelor's or master's), as authored by a student at Eindhoven University of Technology. Student theses are made available in the TU/e repository upon obtaining the required degree. The grade received is not published on the document as presented in the repository. The required complexity or quality of research of student theses may vary by program, and the required minimum study period may vary in duration.

General rights
Copyright and moral rights for the publications made accessible in the public portal are retained by the authors and/or other copyright owners and it is a condition of accessing publications that users recognise and abide by the legal requirements associated with these rights.

- Users may download and print one copy of any publication from the public portal for the purpose of private study or research.
- You may not further distribute the material or use it for any profit-making activity or commercial gain

TU/e technische universiteit eindhoven

FOM-Instituut voor Plasmafysica Rijnhuizen

Forschungszentrum Jülich
in der Helmholtz-Gemeinschaft

Helium transport and exhaust measurements with an ITER-relevant spectroscopic technique

J.E. Boom

October 2007 PMP 07-16

Supervision: dr. R.J.E. Jaspers
prof. dr. N.J. Lopes Cardozo

Acknowledgments

The first words of appreciation I would like to address to my supervisors Niek Lopes Cardozo and Roger Jaspers: thanks to both of you for giving me the opportunity to fulfil my traineeship as part of the FOM Rijnhuizen team located at TEXTOR (Forschungszentrum Jülich). All your comments and support have been of great help in keeping my enthusiasm high.

Secondly, I would like to express my gratitude to those who introduced me to the wonderful field of Charge eXchange Recombination Spectroscopy. To Maarten De Bock, Roger Jaspers, Manfred von Hellermann, Fenton Glass, Ephrem Delabie, and Sergei Tugarinov: thanks for showing me the light.

Since keeping a tokamak up and running is a group enterprise, which has been vital for the accomplishment of this work, I would like to thank the whole TEXTOR team for their efforts.

My acknowledgments would not be complete without commemorating the infamous Dutch coffee table with its Tuesdays ≡ Cakedays. The witty, sarcastic, cheerful, ironic, futile, jolly, cynical, and vivid discussions that flew across the table (and usually had nothing to do with physics) were a welcome daily time-out to me. Apart from those already mentioned, I would like to also thank for that Ivo, Marco, Cor, Ben, Egbert, Tony, Serge, Geert-Willem, Jon, Andreas, Lie Ming, Cor, Hans, Bart, Diego, Jarich, and all the people who came by for a visit.

Abstract

In the ongoing search for (re)new(able) energy sources, the approach of gaining energy from the fusion reaction of two nuclei is very challenging from a physics point of view. The released energy of about 17.6 *MeV* originates from the fusion of the hydrogen isotopes deuterium (D) and tritium (T), and it comes in the form of an α-particle (i.e. fast helium) and a neutron. In trying to maintain an effective fusion process, there is an important role for helium. Its concentration is regulated by the delicate balance between maintaining α-particles long enough to release their energy to the bulk plasma and removing the slowed-down helium particles quick enough at the plasma edge in order to avoid suffocation. This balance is manifested in the Reiter criterion $\rho \equiv \tau^*_\alpha / \tau_E \leq 9$, which relates the global particle confinement time τ^*_α to the energy confinement time τ_E.

Monitoring the behaviour of thermal helium in the plasma is the main subject considered in this thesis, which is done by performing helium injection experiments on the TEXTOR tokamak. Based on this type of experiment, the following topics are addressed: first, three methods for measuring the helium density in the plasma are compared. Using the method of combined charge exchange recombination and beam emission spectroscopy (CXRS and BES), properties as the global helium confinement time and diffusion and convection coefficients are then derived from these density measurements. Finally, the Dynamic Ergodic Divertor (DED) at TEXTOR was used to increase the perturbation on the magnetic field lines in the plasma edge and hence influence the helium recycling efficiency and its effective confinement time (the key parameters in helium exhaust experiments).

As a main result it has been shown that measuring helium densities with the combined CXRS and BES method can be performed with good agreement to the method using a beam density calculation (with the charge exchange analysis package, CHEAP) and a quick estimate from electron density measurements. By comparing the density measurements to the results from numerical modelling, the diffusion and convection coefficients can separately be derived during the transient phase of the helium injection (and their ratio can be obtained from the steady-state phase). Since the Reiter criterion was not attained for standard TEXTOR conditions, an initial attempt was made to reduce the helium confinement time by applying the DED. Due to a non-optimized configuration for helium pumping, the intended effects have not been observed. For ITER however, where the divertor configuration has much better prospects for helium pumping, the analysis and control of the helium ash remains indispensable and the present work is a step in that direction.

Contents

Abstract v

Contents vii

1 Introduction 1
- 1.1 Nuclear fusion 1
- 1.2 The role of helium 2

2 Theory 5
- 2.1 Helium concentration and transport 5
  - 2.1.1 Lawsons criterion and burn conditions 5
  - 2.1.2 Transport properties and particle confinement 8
- 2.2 Charge eXchange Recombination Spectroscopy 11
  - 2.2.1 Basic principles 11
  - 2.2.2 Additional processes and cross-section effects 13
  - 2.2.3 Beam Emission Spectroscopy 15

3 Experimental setup 19
- 3.1 TEXTOR and its supporting systems 19
  - 3.1.1 The TEXTOR tokamak 19
  - 3.1.2 Utilized plasma diagnostics 21
  - 3.1.3 The Dynamic Ergodic Divertor 22
- 3.2 CXRS diagnostics 24
  - 3.2.1 Equatorial lines-of-sight and the top-view ITER-pilot system 24
  - 3.2.2 Spectrometer setups 26

4 Helium spectral analysis 29
- 4.1 Characteristics of the helium spectrum 29
- 4.2 Measuring a density profile 33
  - 4.2.1 Estimate by means of electron density 33
  - 4.2.2 Profile calculations performed with CHEAP 34
  - 4.2.3 Using CXRS and BES for determining helium density profiles 36
  - 4.2.4 Comparison and discussion 39

5 Helium transport 41
- 5.1 Determining transport coefficients 41
  - 5.1.1 Diffusion and convection in the transient phase 41
  - 5.1.2 Transport coefficients in steady state 43
  - 5.1.3 Intermediate comparison and discussion 45
- 5.2 The effect of the DED on helium confinement 45

6 Conclusions 49
- 6.1 On the behaviour of helium 49
- 6.2 Outlook 51

Bibliography 53

Chapter 1

Introduction

1.1 Nuclear fusion

In the ongoing search for (re)new(able) energy sources, the approach of gaining energy from the fusion reaction of two nuclei is very challenging from a physics point of view. The released energy originates from the difference in binding energies of the fusion fuel and products. It can be calculated from the mass defect that the fusion reaction results in, using (from [1])

$$E = mc^2\ . \qquad (1.1)$$

The fusion of the hydrogen isotopes deuterium (D) and tritium (T), as shown in (1.2), is the one that initially will be exploited. Where typical exothermic chemical reactions produce about 1 eV (= $1.6 \cdot 10^{-19}$ J) of energy, the D-T reaction releases about 17.6 MeV:

$${}^{2}_{1}D + {}^{3}_{1}T \rightarrow {}^{4}_{2}He\,(3.5\,MeV) + {}^{1}_{0}n\,(14.1\,MeV)\ . \qquad (1.2)$$

In order to make the fusion reaction happen, the repelling Coulomb force that the positively charged D and T nuclei exert on each other has to be overcome. For the D-T reaction this barrier can be surmounted by raising the temperature (i.e. increasing the thermal energy of the nuclei) to about 120 million K, which equals about 10 keV. At these high temperatures the gas mixture becomes fully ionised, so electrons and ions are no longer bound to each other and form a plasma. This separation in electrically charged particles provides the opportunity to magnetically confine the plasma, since charged particle movement perpendicular to magnetic field lines is limited by the Lorentz force. Figure 1.1 shows the main components of the so-called tokamak configuration, a widely used concept for magnetic confinement.

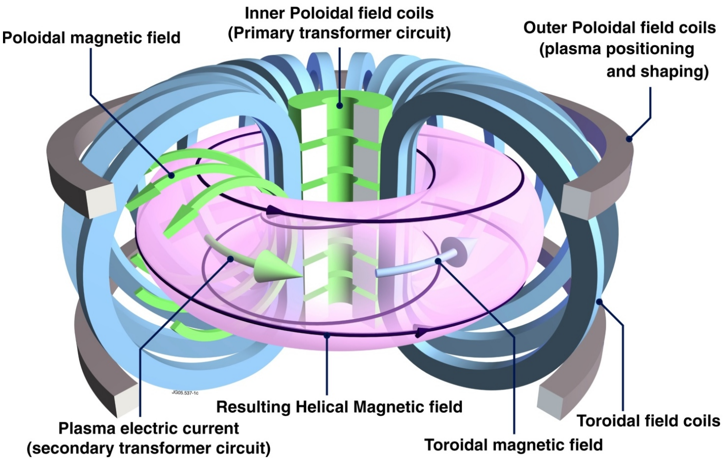
Inner Poloidal field coils
(Primary transformer circuit)
Poloidal magnetic field
Outer Poloidal field coils
(plasma positioning
and shaping)
Resulting Helical Magnetic field
Plasma electric current
(secondary transformer circuit)
Toroidal field coils
Toroidal magnetic field

Figure 1.1 : *Basic elements of a tokamak: the inner poloidal field coils induce a toroidal plasma current, and consequently a poloidal magnetic field. Combined with the toroidal field this results in a helical magnetic field. (image: JET-EFDA)*

Since charged particle movement along magnetic field lines is hardly limited, the closure of magnetic field lines on themselves leads to the toroidal shape of the vacuum vessel that contains the plasma. The toroidal magnetic field lines in Figure 1.1 are produced by the toroidal field coils placed around the vessel. A poloidal component also needs to be given to the magnetic field in order to prevent charge separation and plasma loss due to $\vec{E}\times\vec{B}$, curv $\vec{B}$, and grad $\vec{B}$ drifts, which would occur in case of just a toroidal magnetic field. The poloidal magnetic field lines are a result of an induced current in the plasma (which contributes to heating the plasma as well via Ohmic dissipation). This is done by using the plasma as the secondary circuit of a transformer, where the primary circuit is formed by the inner poloidal field coils. The combination of the toroidal and poloidal magnetic fields leads to the helical field lines that confine the plasma, as shown in Figure 1.1. The outer poloidal field coils are mainly used for controlling the plasmas position and shape, their vertical magnetic field induces a force compensating the plasmas outward hoop force.

1.2 The role of helium

The helium producing fusion reaction (1.2) is not only chosen for its large energy release, but it also has the highest cross-section at relatively low temperatures. The fusion cross-section $\sigma(E)$ expresses the probability of passing the Coulomb barrier; its average over the relative velocities v is plotted as a function of temperature in the right graph of Figure 1.2, where the maximum is found at about 100 keV [2]. Due to quantummechanical effects (tunnelling) in surpassing the Coulomb barrier and the fact that there is a significant amount of fast particles in the Maxwellian tail of the velocity distribution, the fusion reaction is already possible at temperatures of about 10 keV (as previously mentioned in paragraph 1.1).

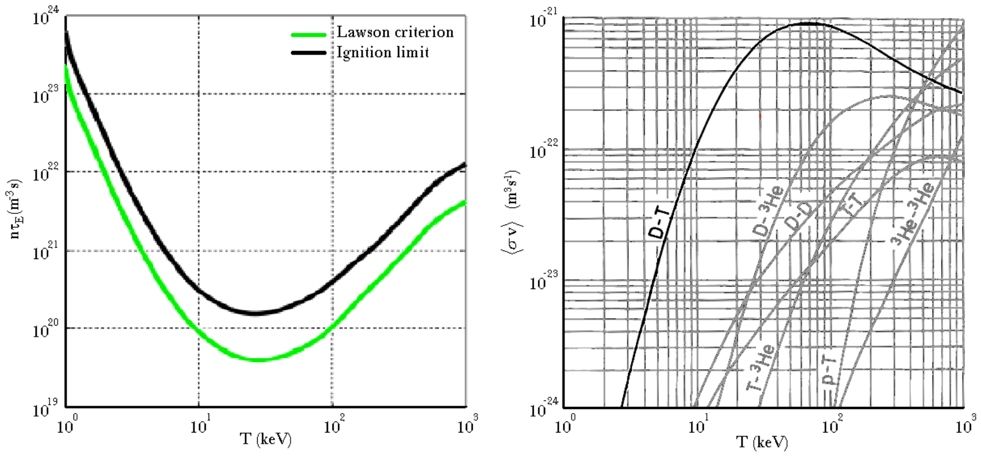

Figure 1.2 : *In the right graph the average of the fusion cross-section over the relative velocities is plotted as a function of temperature for several possible fusion reactions. The left graph shows Lawsons criterion and the ignition limit for the D-T reaction, which must be met in order to have an efficient fusion process.*

In order for the reaction (1.2) to happen, it is not sufficient to just reach the high temperatures of the right graph of Figure 1.2. A second requirement is that D and T should collide frequently, therefore the particle density n has to be adequately high as well. As a third constraint, the plasma energy should be confined long enough to sustain the fusion reaction (i.e. not cool down), so it demands a minimum energy confinement time τ_E. In order to sustain an efficient fusion process these three conditions must be met simultaneously [3], as is stated here by Lawsons criterion (which will be derived in detail in the next chapter, section 2.1.1):

$$n\tau_E T > 1.5\cdot 10^{21}\ keV m^{-3} s\,. \tag{1.3}$$

In the left graph of Figure 1.2 the confinement quality $n\tau_E$ has been plotted as a function of temperature for the *D*-*T* reaction, where the minimum condition described by Lawsons criterion is shown as the green curve. The same graph also shows the even more severe requirement for so-called 'ignition' (where the ratio *Q* of fusion power to input power reaches infinity and the fusion reaction is self-sustaining), which has a triple product value of

$$n\tau_E T > 5\cdot 10^{21}\ keV\,m^{-3}s\,. \tag{1.4}$$

In trying to reach an ignited plasma, there is an important role for the helium produced in (1.2). On the one hand it is desirable that the highly energetic α-particles (3.5 *MeV*) remain long enough in the plasma to transfer all their energy, so the plasma is maintained at high enough temperatures and *Q* retains infinity. On the other hand, the power loss due to Bremsstrahlung radiation is four times as much for the α-particles as it is for the replaced *D* and *T* fuel particles together (since it is proportional to Z^2, with Z the particles charge number). Furthermore, the helium presence in the plasma is a dilution to the concentration of the fuel products *D* and *T*. This means that a too high helium concentration could rapidly terminate the ignited condition of the plasma.

Analogue to a burning flame, a plasma burning in steady state therefore requires a sufficient thermal insulation (quantified by τ_E) and, at the same time, sufficient particle throughput by convection and diffusion (related to the global particle confinement time τ^*_α). In the specific case of helium ash, it is possible to relate the mechanisms of particle and energy loss to each other since both originate from the same source. Taking this into account reduces the ignition limits in the left graph of Figure 1.2 even further [4], and can be associated to the criterion:

$$\rho \equiv \frac{\tau^*_\alpha}{\tau_E} \leq 9\,. \tag{1.5}$$

As it emerges from the introduction above, the role of helium in a burning plasma is both critical and complex. Its concentration is regulated by the delicate balance between maintaining fast α-particles long enough to lose their energy and removing the slowed-down helium particles quick enough at the plasma edge in order to avoid suffocation. The energetic α-particles create interesting physical challenges of their own as well; e.g. they are known to excite global Alfvén waves (so-called Toroidal Alfvén Eigenmodes), which may cause considerable losses of α-particles on their subsequent destabilisation [5]. In this thesis however, monitoring the behaviour of thermal helium in the plasma is the main subject to be considered. This will be done by addressing the following three questions:

1. **What are the possibilities for measuring helium densities?**
2. **Can helium transport coefficients be derived from these measurements?**
3. **Is there a way to manipulate the behaviour of helium?**

In Chapter 2, the conduct of helium in the plasma will first be discussed in more detail than in this introduction; it is followed by some basic theoretical aspects of spectroscopy, the means by which helium will be observed. The features of the TEXTOR tokamak, on which the experiments have been performed, and the (spectroscopy) setups will be treated in Chapter 3. In Chapter 4, the answers to the first question are investigated by regarding the helium spectrum and comparing three different ways to obtain helium density profiles. The answer to the second question will be explored in the first part of Chapter 5, where the density profiles (as measured in Chapter 4) are used to obtain the helium transport coefficients for convection and diffusion. In the second part of Chapter 5, the results will be discussed of experiments aiming to influence the helium behaviour by changing the plasma edge conditions.

Chapter 2

Theory

In order to be able to investigate the questions posed in paragraph 1.2, this chapter explicates the theoretical background against which the experiments of Chapter 4 and Chapter 5 have been performed. The first paragraph of this chapter is strongly related to the importance of helium as mentioned in Chapter 1. It describes the conditions of helium in the plasma and introduces some basic helium transport properties. In the second paragraph, the theoretical aspects behind charge exchange recombination and beam emission spectroscopy are introduced. These are the main measurement techniques that will be used in order to answer the questions posed at the end of paragraph 1.2.

2.1 Helium concentration and transport

The important role the helium concentration plays in achieving an ignited plasma becomes clear in the first section of this paragraph. Lawsons criterion, that was posed in the introduction, is quickly derived here and extended towards burning conditions that are determined by the helium concentration and its confinement time. In the second section a basic model is described that relates the global helium confinement time to the plasma boundary and pumping conditions.

2.1.1 Lawsons criterion and burn conditions

Following [6], Lawsons criterion is swiftly derived from the power balance of the thermonuclear fusion reaction of (1.2). The total power going out of the plasma (P_{out}) is defined as the sum of the produced fusion power P_{fusion} and the power P_{loss} leaving the plasma via energy losses. The fusion power per unit volume is the product of the ion densities n_D and n_T (while assuming that $n_D = n_T = \frac{1}{2}n$), the reactions cross-section $\langle \sigma v \rangle_{D-T}$ from Figure 1.2, and the released energy E per fusion reaction (1.2):

$$P_{fusion} = \frac{n^2}{4} \langle \sigma v \rangle_{D-T} E \,. \tag{2.1}$$

The loss power is the sum of the radiation loss due to Bremsstrahlung ($\sim n^2\sqrt{T}$) and all other (transport) power losses in terms of the plasma energy density ($\sim nT$). Taking the sum of electrons and ions into account for the latter, and a characteristic energy confinement time τ_E, it follows for the loss power that

$$P_{loss} = P_{Brems} + P_{transport} = \alpha n^2 \sqrt{T} + \frac{2 \cdot \frac{3}{2} nT}{\tau_E} \,. \tag{2.2}$$

With an efficiency η for the amount of P_{out} that can be used again for heating the plasma, the Lawson criterion states that $\eta P_{out} > P_{loss}$ so that there is a net gain of energy for the process as a whole. With the use of the temperature dependent cross-section values, $\alpha = 3.8\cdot10^{-29}\ J^{1/2}m^3s^{-1}$, $E = 17.6\ MeV$, and Lawsons choice of $\eta = 1/3$ it follows from this inequality that

$$n\tau_E > \frac{3T}{\frac{\eta}{1-\eta}\cdot\left(\frac{1}{4}\left\langle\sigma v\right\rangle_{D-T}E\right)-\alpha\sqrt{T}} > 6\cdot10^{19}\ m^{-3}s\,. \tag{2.3}$$

The value of $6\cdot10^{19}\ m^{-3}s$ is the absolute minimum of $n\tau_E$ as it is found in Figure 1.2 at a temperature of about 25 *keV*. For the temperature range around this minimum, the approximation of $\left\langle\sigma v\right\rangle_{D-T} \sim T^2$ is valid. Using this in (2.3), the fusion 'triple product' introduced in 1.2 is calculated to be $1.5\cdot10^{21}\ m^{-3}s\ keV$.

In order for the plasma to be truly 'ignited', Lawsons criterion must be narrowed even more. This means that the power loss P_{loss} should be fully covered by the α-particle power P_α which originates from (1.2), so that no power has to be coupled back into the plasma. At this high temperatures the Bremsstrahlung in (2.2) can be neglected, and with $E_\alpha = 3.5\ MeV$ in $P_\alpha = \frac{n^2}{4}\left\langle\sigma v\right\rangle_{D-T}E_\alpha$ the ignition requirement $P_\alpha > P_{loss}$ results in:

$$n\tau_E > \frac{12T}{\left\langle\sigma v\right\rangle_{D-T}E_\alpha} > 1.5\cdot10^{20}\ m^{-3}s\,. \tag{2.4}$$

Using the same approximation for the effective *D-T* cross-section again, the minimum $n\tau_E$ of $1.5\cdot10^{20}\ m^{-3}s$ results in a triple product value of $5\cdot10^{21}\ m^{-3}s\ keV$. This corresponds to the raised ignition condition as it has already been shown in Figure 1.2.

As is shown in [4], the α-particle power P_α is strongly correlated to the helium concentration, and the earlier assumption of $\frac{1}{2}n = n_D = n_T$ is no longer valid. Taking this into account, the conditions for an efficiently burning plasma are even further reduced than the ignition limit of (2.4). In the rest of this section, the approach of [4] is followed in order to demonstrate the importance of the helium concentration f_{He} and, with that as well, the importance of the ratio between the global helium particle confinement time and that of energy.

For a start, the following simplifications are assumed:

- the plasma has a uniform temperature, i.e. $T = T_e = T_i = T_{He} = T_Z$;
- deuterium and tritium densities are equal ($n_D = n_T$ as before) and $n_i = n_D + n_T$;
- E_α, produced in (1.2), is completely transferred to the plasma, i.e. all α-particles are entirely thermalised;
- there exists only one impurity species next to the helium ash, it is of low nuclear charge number Z and hence fully ionized at temperatures of the order of 10 *keV*;
- the pressure from fast α-particles p_α is neglected in the energy balance.

Using these simplifications, the definitions of concentration $f_{He} = n_{He}/n_e$ and $f_Z = n_Z/n_e$, and the quasi-neutrality assumption it is possible to derive the dilution parameter f_i:

$$f_i = \frac{n_i}{n_e} = 1 - Zf_Z - 2f_{He}\,. \tag{2.5}$$

Together with the total particle density ($n_{tot} = n_e + n_i + n_{He} + n_Z = n_e f_{tot}$), this gives the possibility to rephrase the power balance $P_\alpha = P_{loss}$ for the ignition condition in terms of f_i and f_{tot}:

$$n_e\tau_E = \frac{\frac{3}{2}f_{tot}T}{\frac{1}{4}f_i^2\left\langle\sigma v\right\rangle_{D-T}E_\alpha - R_{rad}(T, f_Z, f_{He})}\,. \tag{2.6}$$

In this case P_{loss} is defined as the sum of $P_{transport} = \frac{3}{2} n_e T f_{tot} / \tau_E$ and $P_{rad} = n_e^2 \cdot R_{rad}(T, f_Z, f_{He})$, which slightly differs from (2.2). The direct relation between the power density P_α and f_{He} follows from the α-particle balance (and shows their dependency on T as well):

$$\frac{n_e^2 f_i^2}{4} \left\langle \sigma v \right\rangle_{D-T} = \frac{n_{He}}{\tau_\alpha^*} . \tag{2.7}$$

Here τ^*_α is the global helium particle confinement time; relating that to the energy confinement time via $\rho \equiv \tau^*_\alpha / \tau_E$ (cf. (1.5)), and expressing n_{He} in terms of f_{He}, the helium particle balance (2.7) simplifies to

$$n_e \tau_E = \frac{4 f_{He}}{\rho f_i^2 \left\langle \sigma v \right\rangle_{D-T}} . \tag{2.8}$$

Combining the results of (2.5), (2.6), and (2.8) it is possible to derive a cubic equation for f_{He}, which can be solved using so-called Cardanos formulas:

$$a_0 + a_1 f_{He} + a_2 f_{He}^2 + a_3 f_{He}^3 = 0 \qquad ; \quad a_i \sim \left(\rho, T, Z, f_Z, E_\alpha, R_{rad} \right) . \tag{2.9}$$

Generally, there are three solutions to this equation, of which the two physically relevant ones for f_{He}, i.e. $0 \leq f_{He} \leq \frac{1}{2}(1 - Z f_Z)$, are shown below in Figure 2.1.

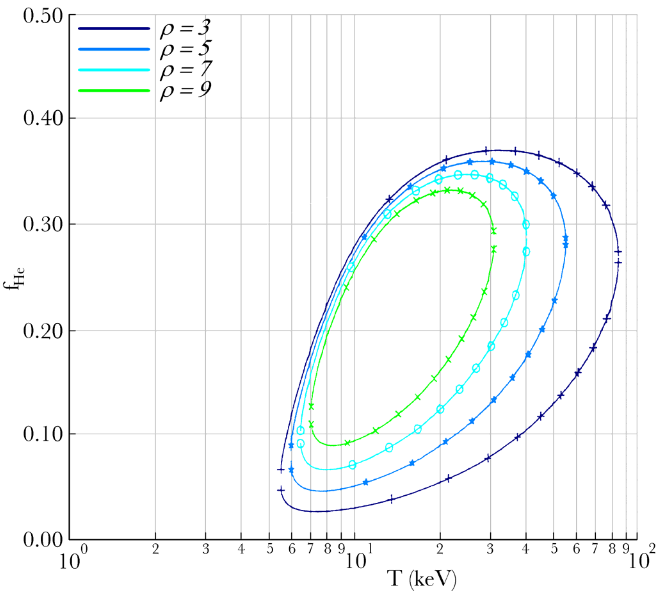

Figure 2.1 : *The physically relevant solutions for (2.9), adapted from* [4], *showing the relative helium concentration f_{He} as a function of temperature T for different values of the confinement time ratio ρ.*

In the so-called low f_{He} mode, which is limited by the confinement restriction (Lawson criterion), the helium concentration is about 5-15 %. Concentrations of 15-25 % are found in the high f_{He} mode, which is restrained by the dilution/radiation limit. The explicit accounting for the radiation losses results in the low and high temperature limits. But even when these are neglected, the restraints on the high f_{He} mode still appear when just the dilution effects are consistently taken into account.

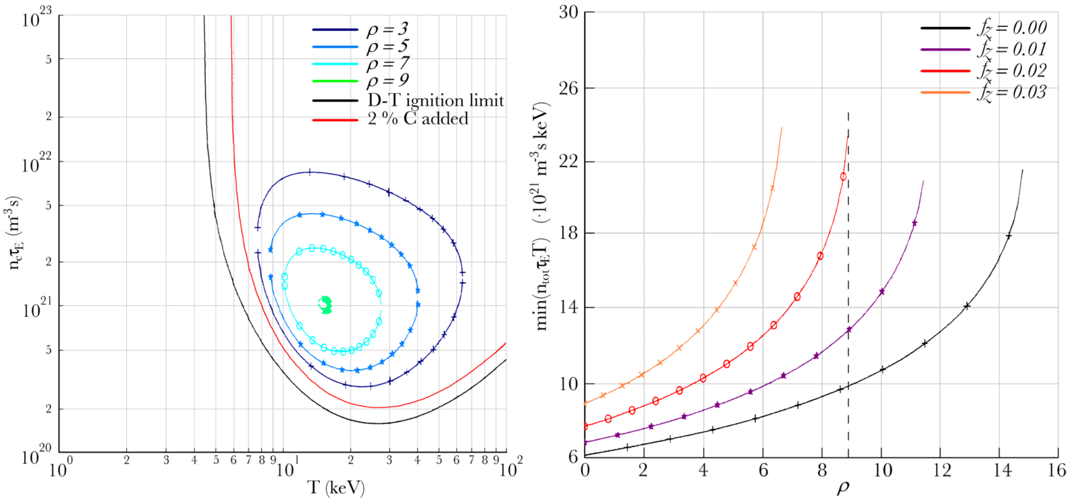

Figure 2.2 : *Influence of confinement time ratio and impurity concentration on the ignition values, adapted from* [4]. *In the left graph the ignition area is plotted for different* ρ. *The right graph shows rapidly increasing triple product values for increasing carbon concentration.*

The influence of the confinement time ratio ρ on the f_{He} restrictions is already shown in Figure 2.1, but as it is an important parameter in (2.9), it also has a direct effect on the ignition condition. This effect is shown in the left graph of Figure 2.2, where several ρ-contours are plotted for the ignition condition of a *D-T* fusion reaction in the presence of a carbon impurity content of $f_Z = 0.02$. It is clearly seen in that graph that the temperature range for which ignition is possible vanishes beyond a critical confinement time ratio where the ρ-contour has reduced in size to a singular point. When radiation losses are taken into account in τ_E, as is suggested in [7], the area of the ρ-contours becomes even smaller than shown in the left graph of Figure 2.2.

The minima of the *D-T* ignition limits for $f_Z = 0.00$ and $f_Z = 0.02$ in the left graph correspond to the respective $\rho = 0$ cases in the right graph of Figure 2.2. As a consequence of the temperature dependence of dilution and radiation losses, the minimum temperature for the ignition limit decreases with increasing ρ. However, as is shown in the right graph of Figure 2.2, the overall minimum of the triple product rises since $n_e\tau_E$ increases dramatically. Taking the influence of impurities into account, it is also seen in that graph that $\rho_{critical}$ is about 9 in case of a carbon dilution of 2%, and becomes even smaller for higher carbon impurity values.

The next section considers the transport properties of helium, which can be derived from gas puffing experiments. From these types of experiments it is also possible to determine the helium confinement time in ρ, which is strongly related to plasma boundary conditions.

2.1.2 *Transport properties and particle confinement*

In this section it is described how the helium transport properties of radial diffusivity and convective velocity can be determined from gas puffing experiments. In Figure 2.3 the time-evolution of such an experiment is illustrated, which essentially shows the injection of helium and the subsequent rise and decay of its density. The time evolution of the helium density is described by the flux-surface averaged radial diffusion equation, adapted from [8]:

$$\frac{\partial n_{He^{2+}}(r,t)}{\partial t} = -\nabla\cdot\left(\Gamma_{He^{2+}}(r)\right) + S_{He^{2+}} \,. \tag{2.10}$$

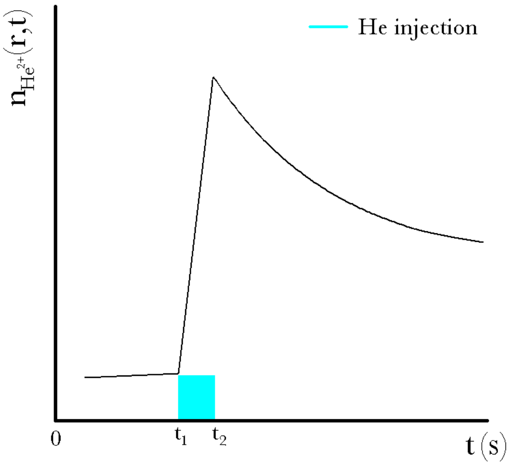

Figure 2.3 : *Illustration of a helium gas injection experiment, where a vast amount of helium is injected from t_1 until t_2 and subsequently decays exponentially.*

In (2.10) the helium sources within the observed volume are denoted as S_{He}, and $\Gamma_{He}(r)$ is the radial flux density in terms of the normalized radius in toroidal flux coordinates. The flux density follows from particle conservation, with the use of the diffusivity $D(r)$ and convective velocity $V(r)$:

$$\Gamma_{He^{2+}}(r) = -D\cdot\nabla\left(n_{He^{2+}}(r,t)\right) + V\cdot n_{He^{2+}}(r,t)\,. \tag{2.11}$$

Assuming that a source-free volume in the plasma is observed ($S_{He} = 0$), where all helium is fully ionized, it is possible to solve this set of equations. In the transient case, e.g. during the injection of helium, the left hand side of (2.10) is not equal to zero and it follows for $\Gamma_{He}(r)$ that

$$\Gamma_{He^{2+}}(r) = -\frac{1}{r}\int_0^r r'\frac{\partial n_{He^{2+}}(r',t)}{\partial t}\mathrm{d}r'\,. \tag{2.12}$$

Using the time derivative of the helium density, obtained from measurements during an experiment such as shown in Figure 2.3, $\Gamma_{He}(r)$ can be determined in this way. If these n_{He} measurements are simultaneously performed at different radii, this can be used to obtain a density profile. From such a density profile, exemplified in the left graph of Figure 2.4, the density gradients $\nabla n_{He}(r,t)$ from (2.11) can be calculated. So, from the combination of such measurements of $\Gamma_{He}(r)$ and $\nabla n_{He}(r,t)$, the transport coefficients D and V can be calculated separately as shown in the right graph of Figure 2.4.

In steady state $\Gamma_{He}(r) = 0$, so only the ratio of the transport coefficients D and V can be determined, as follows directly from (2.11):

$$\frac{\nabla n_{He^{2+}}}{n_{He^{2+}}} = \frac{V(r)}{D(r)} \quad ; \qquad \Gamma_{He^{2+}}(r) = 0\,. \tag{2.13}$$

Using either of these approaches, it will be possible to derive the helium transport coefficients from density profile measurements and accordingly answer the second question posed in 1.2.

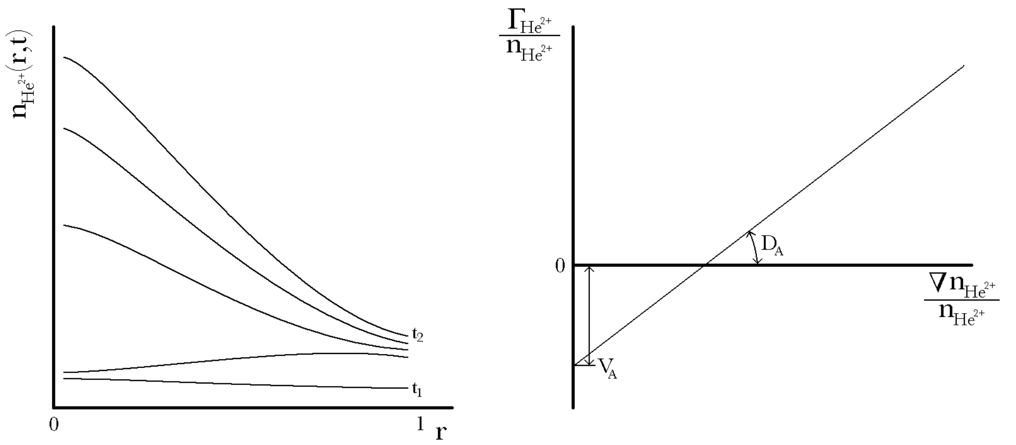

Figure 2.4 : *The left graph shows an illustration of helium density profiles as a function of the normalized radius for a few instants during the injection phase in Figure 2.3. The right graph shows how the transport coefficients D_A and V_A can be determined using (2.11).*

After the helium injection phase in Figure 2.3 has ended, the radial gradients in the density profiles of Figure 2.4 will not change anymore during the pump out period that follows. Its shape is namely determined by the transport coefficients D and V, and the height follows from the amount of helium present [8], [9]. This profile invariance provides the possibility of obtaining the characteristic time τ^*_α for basic helium transport processes, and consequently makes a method available for calculating ρ in (1.5). The global α-particle confinement time τ^*_α is defined as

$$\tau^*_\alpha \equiv \frac{N_\alpha}{\Phi_\alpha} = \frac{N_\alpha}{\Phi_{\alpha,out} - \Phi_{\alpha,return}} = \frac{N_\alpha}{\Phi_{\alpha,out}\left(1-\mathrm{R}_{eff}\right)} = \frac{\tau_\alpha}{\left(1-\mathrm{R}_{eff}\right)}. \tag{2.14}$$

The number of α-particles is denoted here as N_α and Φ_α represents the net flux of the α-particles leaving the volume in which they were confined. It follows directly from the definition that τ^*_α can be determined from the exponential decay shown in Figure 2.3, since:

$$N_\alpha(t) \sim \exp\left(-\frac{t}{\tau^*_\alpha}\right). \tag{2.15}$$

In (2.14) the effective recycling coefficient R_{eff} is defined as the ratio of the returning α-particle flux $\Phi_{\alpha,return}$ to the outward flux $\Phi_{\alpha,out}$, i.e. $R_{eff} = \Phi_{\alpha,return}/\Phi_{\alpha,out}$. For burning plasmas, it has been suggested in [4] to make a distinction between the plasma core region (fast α-particle creation) and the plasma edge (region of thermalised α-particle reflection and pump out). This results in an amended definition of τ^*_α, using $\tau_{\alpha 1}$ for the internal α-particle confinement time and $\tau_{\alpha 2}$ for the mean residence time in the plasma boundary region:

$$\tau^*_\alpha = \tau_{\alpha 1} + \tau_{\alpha 2} \cdot \frac{R_{eff}}{\left(1-R_{eff}\right)}. \tag{2.16}$$

The significance of $\tau_{\alpha 2}$ in τ^*_α is determined by the factor $R_{eff}/(1-R_{eff})$ which is the mean number of recycling events that an α-particle experiences before it is being pumped away. Because helium is a noble gas, R_{eff} will be close to unity for all (pump)surfaces in the plasma edge region. As a result, since $(1-R_{eff})$ is in the denominator, small variations of R_{eff} will already have a large effect on τ^*_α. Obviously, the transport properties of $\tau_{\alpha 1}$ and $\tau_{\alpha 2}$ are coupled (at the screening layer), and both have to be optimized in order to reach the burning condition. Note that the definition of (2.16) becomes identical again to the last equality in (2.14) when $\tau_{\alpha 1} = \tau_{\alpha 2}$. This approach is justified for plasmas with no burning core [10], so it applies to most of the currently performed experiments.

In previous studies at TEXTOR concerning the global particle confinement time τ^*_α, experiments have been carried out making use of the effect of pumping, where R_{eff} is found to vary between 1.00 and 0.92 depending on the amount of active pumps [11]. More recently also, the influence of magnetic islands on (impurity) transport has been investigated [12]. The experiments described here in Chapter 5 are utilizing the Dynamic Ergodic Divertor (DED), a special feature of the TEXTOR tokamak. In these experiments it is intended (cf. [13]) to vary R_{eff} by changing the impact of the DED on the plasma edge, hence altering τ^*_α.

The next paragraph is used for explaining the basic theory behind the spectroscopic techniques used for observing the behaviour of helium (mainly its density) in such transport experiments as described above.

2.2 Charge eXchange Recombination Spectroscopy

A very powerful tool for obtaining information on the conduct of impurities in a plasma is charge exchange recombination spectroscopy (CXRS) [14]. It is based on line-emission by excited ions, and its strength is the fact that it provides local measurements of important plasma parameters such as the temperature, velocity, and density of the monitored impurity. The theoretical background of this technique is described in this paragraph, in a similar manner to [15] but specified to the observation of helium. It is introduced in the first section, and in the second section some details and complicating effects are explained. In the last section, the use of beam emission spectroscopy (BES) as an additional tool is described.

2.2.1 *Basic principles*

In the plasma core, all (light to medium weight) impurity ions are fully stripped from their electrons due to the high temperatures. In order for these ions to send out line-emission, they have to capture an electron in an excited state. This electron can be received from neutral particles (e.g. injected by a neutral beam) in a charge exchange reaction, which is then captured in a high quantum level. The excited ion will loose its energy and cascade down to the ground state by emitting light at several (visible) wavelengths. When helium is the observed impurity ion, the charge exchange reaction is expressed as

$$He^{2+} + H^0 \overset{CX}{\rightarrow} \left(He^{1+}\right)^* + H^+ \rightarrow \left(He^{1+} + h\nu_1 + h\nu_2 + \ldots\right) + H^+ \,. \tag{2.17}$$

For the excited $(He^{1+})^*$ ions in (2.17), the $n = 4 \rightarrow 3$ transition is the dominant transition in the visible spectrum (it is prevailing over the $\Delta n = 2$ transitions at 320 *nm* and 468 *nm*) [16]. The emission from $n = 4 \rightarrow 3$ is usually referred to as HeII emission, its natural wavelength and line width are respectively given by $\lambda_n = 468.5$ *nm* and $\Delta\lambda_n \approx 10^{-5}$ *nm* [17].

For interpretation of the perceived line-emission, a Cartesian observation system is defined with the z-axis in the direction of the line-of-sight (l.o.s.), see Figure 2.5. If an ion moves towards the observer with a velocity u_z, determined by a thermal energy of e.g. 10 eV, the perceived Doppler-shift in the line-emission is given by

$$\Delta\lambda_D = u_z \cdot \frac{\lambda_n}{c} = 3 \cdot 10^{-2}\, nm \gg \Delta\lambda_n \,. \tag{2.18}$$

The result of (2.18), where c is the speed of light, allows for the line-emission to be described by a delta-function because the thermal energy in tokamak plasmas exceeds 10 eV by far.

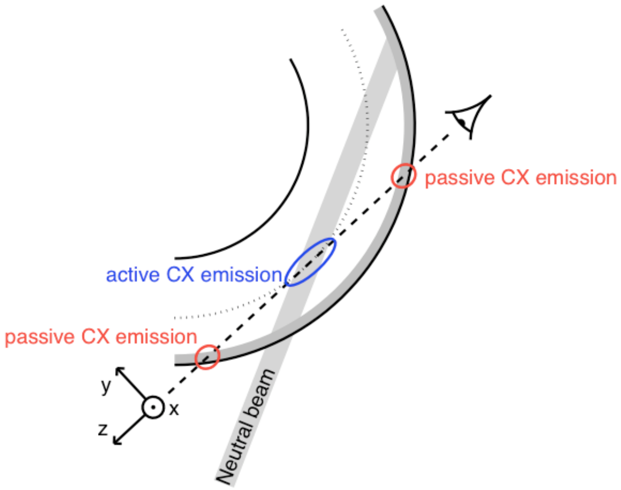

Figure 2.5 : *Cartesian observation system for CX emission in a tokamak, with the z-axis along the line-of-sight. Indicated are the different sources of CX emission in the edge region and neutral beam. (image:* [15]*)*

In general, the velocity $\bar{u}$ of the helium ions (with mass m_{He} and temperature T_{He}) relative to the helium fluid velocity $\bar{v}$ is represented by a Maxwellian velocity distribution:

$$g\,(u_x, u_y, u_z) = \left(\frac{m_{He}}{2\pi T_{He}}\right)^{3/2} \cdot \exp\left[-\frac{(u_x - v_x)^2 + (u_y - v_y)^2 + (u_z - v_z)^2}{2T_{He}/m_{He}}\right]. \tag{2.19}$$

Regarding a small volume dx·dy·dz, where light is emitted by the moving helium ions in the direction of the observer, the perceived spectrum is then given by

$$\begin{aligned} f_{local}(\lambda) &= \frac{1}{4\pi} n_H n_{He} \iiint \langle \sigma v \rangle_{CX} \cdot \delta\big(\lambda - \lambda_n (1 + u_z/c)\big) \cdot g(\bar{u})\, \mathrm{d}u_x \mathrm{d}u_y \mathrm{d}u_z = \\ &= I \exp\left[-\frac{(\lambda - \lambda_0)^2}{(\Delta\lambda)^2}\right]. \end{aligned} \tag{2.20}$$

As can be seen here, the spectrum of light depends on the density n_H of hydrogen neutrals, the density n_{He} of the helium ions present in the small volume, and the effective emission rate $\langle \sigma v \rangle_{CX}$ for their charge exchange reaction (cf. (2.17)). For the second equality in (2.20), the use of the delta-function that describes the emission line is exploited, which leads to a Gaussian representation. This provides the possibility to obtain the local helium velocity, temperature, and density, which follow respectively from the Gaussians peak position, peak width, and its intensity:

$$\lambda_0 = \lambda_n \left(1 + \frac{v_z}{c}\right), \tag{2.21}$$

$$\Delta\lambda = \sqrt{\frac{2T_{He}}{m_{He}}}\frac{\lambda_n}{c}, \tag{2.22}$$

$$I \ = n_H n_{He}\frac{\langle\sigma v\rangle_{CX}\,\lambda_n}{4\pi^{3/2}\,c\,\Delta\lambda}\,. \tag{2.23}$$

Extending (2.20), the total observed charge exchange spectrum is the integrated sum along the line-of-sight of all the light that is locally emitted. The strength of CXRS, being that it provides local $v_{z,He}$, T_{He}, and n_{He}, appears now when it is realised that the neutral hydrogen density is zero (so $I = n_H = 0$) for the largest part of the observed volume.

During neutral beam injection there are, on the whole, just two regions where $n_H \neq 0$ as can be seen in Figure 2.5. These are the plasma edge and the region where the neutral beam hydrogen particles penetrate the plasma core [18]. In the edge region, there are actually two processes responsible for the excitation of the He^{1+} ion. The first is electron impact, which is the dominant mechanism of the $n = 4$ level excitation at the very cool outer boundary. The He^{1+} ions that are abundantly present there can reach this excitation level by collisions with electrons. This is not a charge exchange reaction, and therefore usually referred to as 'edge emission' in the analysis of CX spectra. In a more intermediate layer, closer to the magnetically confined core, the charge exchange reaction of (2.17) can occur due to the presence of neutral hydrogen streaming from the vessel wall, which leads to so-called passive charge exchange (PCX) emission. When HeII emission from the edge is fully accounted for, e.g. by a method of subtraction or modelling [19], the only remaining component in the charge exchange spectrum is the active component (ACX) resulting from the neutral hydrogen injection:

$$f_{ACX}(\lambda) = \int_{beam} I \exp\left[-\frac{(\lambda-\lambda_0)^2}{(\Delta\lambda)^2}\right]\mathrm{d}z\,. \tag{2.24}$$

Using multiple lines-of-sight, crossing at different radii along the direction of the neutral beam, this provides the strength of CXRS since each intersection produces a local measurement of $v_{z,He}$, T_{He}, and n_{He}. It is assumed here that each l.o.s. crosses the neutral beam tangential to a magnetic flux surface. On these surfaces $v_{z,He}$, T_{He}, and n_{He} remain constant since they are flux functions, so they can be taken out of the integral of (2.24). This means that $v_{z,He}$ and T_{He} are still given by (2.21) and (2.22) respectively, where it is usually taken up that $v_{z,He}$ can be expressed in terms of poloidal and toroidal velocities ($v_{z,He} = v_\varphi\cos(\alpha) + v_\theta\cos(\beta)$, with α and β the angles between the l.o.s. and the toroidal and poloidal direction). For the helium density, measured for the observed volume of the neutral beam, the integral of (2.24) remains and (2.23) turns into the following expression (applicable to each line-of-sight):

$$I \ = n_{He}\frac{\langle\sigma v\rangle_{CX}\,\lambda_n}{4\pi^{3/2}\,c\,\Delta\lambda}\cdot\int_{beam} n_H\,\mathrm{d}z\,. \tag{2.25}$$

2.2.2 *Additional processes and cross-section effects*

It is important to realise that there is also a number of other processes emitting light in the same visible wavelength range as that of the observed CX reactions, some of which will be shortly discussed here. First, the most valuable of these non-CX emissions is that of

Bremsstrahlung, which provides a continuous background intensity to the whole observed spectrum. It is ascribed to the relative movement of charged particles in the plasma, and its intensity in the visible region is given by [6]:

$$\frac{\mathrm{d}I}{\mathrm{d}\lambda} = 3 \cdot 10^{-21} \frac{\overline{g} n_e^2 Z_{eff}}{\lambda \sqrt{T_e}} . \tag{2.26}$$

The electron temperature T_e is here in *keV*, its density n_e is in m^{-3}, and the wavelength λ in *nm*; an approximate value of $2\sqrt{3}/\pi$ can be used for the free-free Gaunt factor $\overline{g}$. Z_{eff} is the average charge of the plasma particles, a measure for the (im)purity of the plasma. The merit of Bremsstrahlung emission is that it can be used for intensity calibration, as will be done in paragraph 4.2.3.

A second effect that can be observed in CX spectra, is the contribution of other impurities that happen to have neighbouring spectral lines. For the emission line of interest, these adjacent lines can either affect the analysis (in case they overlap) or they can be of use for identification (when they do not overlap, they can be used for wavelength calibration). For the HeII emission at λ_n = 468.52 *nm*, wavelength coincidence could arise from BeIV ($n = 8 \rightarrow 6$) emission at 468.52 *nm*, or CIV emission at 468.57 *nm* [18] (beryllium should of course be a wall component in order to be present in the plasma at all!). If the detection range is large enough, the CIII multiplet could be used for wavelength calibration around the HeII emission (it originates from the edge and emits at 464.7 *nm*, 465.0 *nm*, and 465.1 *nm*).

The time an impurity ion is able to hold the electron received in a CX reaction, gives rise to a third, more bothersome effect. If this period is long enough, it is possible that after a first transition (emitting at the observed wavelength), the electron is excited again to its previously occupied level. As the ion is still charged, it continues to move along the magnetic field lines and a second, delayed line-emission can be observed by the same line-of-sight. This secondary, so-called 'plume' emission is more likely to occur for low-Z ions as H^+ and He^{1+}, since they do not have to be excited to high levels [20]. When, instead, the impurity ion gets neutralised in a second CX reaction, it is no longer bound to the magnetic field. It can then move away and be subjected again to all kinds of line-emission; when detected in the l.o.s. this is referred to as 'halo' emission. Another complication that could appear in the observation of CX spectra is that of black-body radiation. This occurs when certain spots inside the vessel heat up and start radiating in the observations line-of-sight, or reflect into it. When the radiation becomes of the order of magnitude of the Bremsstrahlung (at e.g. 2500 *K*, λ_{max} is about 1152 *nm* but part of the black-body emission is already in the visible range).

For burning plasmas, the creation of fast alpha particles (cf. (1.2)) will also introduce a new feature in the observed HeII charge exchange spectrum. The velocity distribution function of these fast particles is strongly anistropic at their creation, and becomes more isotropic in the subsequent slowing-down process. As is shown in [21], the slowing-down helium particles will produce a broad-band pedestal underneath the HeII emission spectrum. Considerable amounts of fast α-particles have not been created in the experiments described in Chapter 4 and Chapter 5, and they will therefore not deform the observed helium CX spectra.

A final concern arises from the fact that the effective CX emission rate $\langle \sigma v \rangle_{CX}$ is not constant as can be seen in Figure 2.6, contrary to what has been assumed for the second equality in (2.20). It is dependent on the collision velocity v_{col} between the injected neutral particle and the (helium) impurity ion, which can be expressed as (cf. [16])

$$v_{col} = \sqrt{v_{beam}^2 + \left(u_x^2 + u_y^2 + u_z^2\right) - 2v_{beam}\left(u_y \cos(\delta) - u_z \sin(\delta)\right)} \ . \tag{2.27}$$

Here, v_{beam} is the velocity of the beam particles, $\vec{u}$ is related as before to the thermal energy of the helium particles in the plasma, and δ is the angle between the neutral beam and the y-axis in the Cartesian coordinates shown in Figure 2.5. From (2.27) it follows that the collision velocity is distributed around v_{beam} due to the Maxwellian velocity distribution of $\vec{u}$ (cf. (2.19)). For the equatorial CX observation geometry at TEXTOR, this collision velocity is plotted beneath the effective emission rate in Figure 2.6. As can be seen there, and follows from the fact that in TEXTOR $v_{beam}(\sim 50\,keV) \gg \vec{u}\,(\sim 1\,keV)$, the distribution of the collision velocity is relatively small so the assumption made in (2.20) is justifiable.

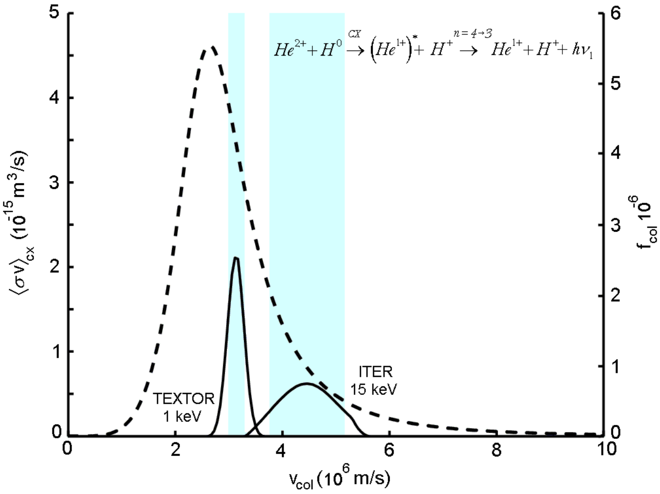

Figure 2.6 : *Effective emission rate for the HeII CX reaction as a function of the collision velocity. Under, the distribution of the collision velocity is plotted for the TEXTOR equatorial viewing geometry, using a plasma temperature of 1 keV and beam energy of 50 keV. For ITER, the collision velocity distribution is calculated for a plasma of 15 keV and using a beam with an energy of 100 keV.*

For ITER, with a much higher thermal energy of the plasma, the dependence of $\langle\sigma v\rangle_{CX}$ on the distribution of collision velocity could potentially lead to a misconception of the observed intensity and Doppler broadening and shift of the emission line. This problem has been surmounted by designing an observation geometry perpendicular to the injected beam, i.e. by making the angle $\delta \approx 0$. The shape of the observed CX spectrum namely depends on u_z, but the collision velocity distribution strongly depends on u_y (since the beam injects in this direction), so the effect on the measured temperature and velocity is negligible [15].

2.2.3 Beam Emission Spectroscopy

Apart from the CX reactions of plasma impurities (2.17) caused by the injection of neutral hydrogen, it is also possible for the beam particles themselves to get excited in a variety of excitation processes before they become ionised in the end. The excited $(H^0)^*$ particles will relax from the $n = 3 \rightarrow 2$ level by Balmer-α emission at a natural wavelength of 656.2 *nm*.

From the frame of reference of the injected hydrogen atoms, the magnetic field that confines the plasma (cf. Figure 1.1) is perceived as an effective Lorentz electric field, given by:

$$\vec{E} = \left(\vec{v}_{beam} \times \vec{B}\right) + \vec{E}_r \ . \qquad (2.28)$$

This perception gives rise to the so-called Motional Stark Effect, i.e. the splitting of energy levels of the beam emission spectrum in a series of Stark components. For the Balmer-α transition of $n = 3 \rightarrow 2$, this results in a splitting up of 15 transitions of which nine emission lines can be resolved [22]. These nine visible emission lines are organised in π- ($\Delta m = 0$) and σ- ($\Delta m = \pm 1$) components [23]. Due to the fact that the neutral beam consists of three species, with respective full, half and one-third energy (see section 3.1.1), the Motional Stark Effect appears three times in the beam emission spectrum, as can be seen in Figure 2.7).

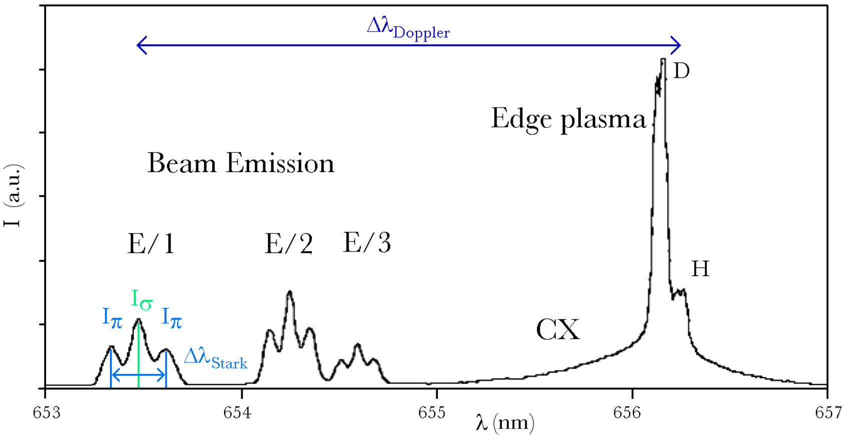

Figure 2.7 : *Balmer-α beam emission spectrum: visible CX emission under the D and H lines and Stark splitting in π- and σ- components of the three beam species.*

The diagnostic applications of the Motional Stark Effect are quite numerous. From the observation of the MSE spectrum, the following parameters can be derived:

- the location of the observed volume (from the Doppler shift $\Delta\lambda_{Doppler}$ of the full energy component, which results from the beam velocity);
- the value of the magnetic field $\vec{B}$ from which the safety factor q can be derived [24] (it results from the Stark splitting $\Delta\lambda_{Stark}$ in π- and σ- components, and their polarisation);
- the direction of the electric field $\vec{E}$ (this follows from the intensity ratio I_π/I_σ of the π- and σ- components);
- the radial electric field $\vec{E}_{rad}$ from (2.28) (which can be derived from polarisation direction differences between two energy components of the neutral beam);
- the fraction of species in the neutral beam (from the intensity ratios $I_E/I_{E/2}$ and $I_E/I_{E/3}$ from the sum of the π- and σ- components for each energy fraction);
- the neutral beam density (from the total intensity I_{BES}, which is the sum over all π- and σ- components of all energy fractions).

It is the last feature that can be very beneficial in obtaining impurity densities, which are to be determined from CX emission described in section 2.2.1. Analogue to the derivation of the CX intensity in (2.25), the intensity of the beam emission spectrum is given by

$$I_{BES}(E) = n_e \frac{\langle \sigma v \rangle_{BES} \lambda_n}{4\pi^{3/2} c \, \Delta\lambda} \cdot \int_{beam} n_H \, \mathrm{d}z \ , \tag{2.29}$$

where the effective emission rate $\langle \sigma v \rangle_{BES}$ takes into account all the possibilities for the excitation of the neutral particles (via Z_{eff}, so the ion collision processes are also included). When this approach is used, observing through the same l.o.s. and accounting for all beam energy fractions, the impurity density follows directly from the division of the CX and BES intensities, and the inconvenient integral of the beam density drops out of the division:

$$n_{He} = n_e \cdot C \sum_{i=1,2,3} \left(\frac{I_{CX}}{I_{BES}} \cdot \frac{\langle \sigma v \rangle_{BES}}{\langle \sigma v \rangle_{CX}} \right)_{E/i} \tag{2.30}$$

This way, the impurity density can be determined with no need for absolute calibration of the optical system, nor for calculation of the beam attenuation, only a calibration factor C is required to account for the different wavelengths of the emission.

Chapter 3

Experimental setup

In this chapter, the instruments are described that are used for performing the experiments of Chapter 4 and Chapter 5. The first paragraph briefly demonstrates the most important aspects of the TEXTOR tokamak (Tokamak EXperiment for Technology Oriented Research) and some plasma affecting and observing systems. In the second paragraph the setup of the CXRS diagnostics is discussed in detail, since this is the main diagnostic used for obtaining helium concentrations.

3.1 TEXTOR and its supporting systems

This paragraph gives in three sections a general description of respectively TEXTOR and its heating systems (ECRH, ICRH, and NBI), the most important diagnostics that are used, and the special features of the Dynamic Ergodic Divertor (DED).

3.1.1 The TEXTOR tokamak

The TEXTOR tokamak is of medium size, with a major and minor radius of respectively 1.75 *m* and 0.47 *m*, and a circular plasma cross section [25]. The toroidal magnetic field B_T is produced by 16 toroidal field coils (see Figure 3.1), and the plasma current is induced by an iron core transformer with six yokes and its poloidal field coils in the centre. Conform the illustration of Figure 1.1, there are also two vertical field coils compensating the hoop force on the plasma, and furthermore TEXTOR has four position control coils for keeping the plasma at the desired position. The maximum achievable values of B_T and I_p are 3.0 *T* and 0.8 *MA*, and the maximum duration of a plasma pulse is 10 *s*; typical values are however more moderate at 2.25 *T*, 0.40 *MA*, and 6 *s*. All main parameters are listed below in Table 3.1.

Table 3.1 : TEXTOR machine and plasma parameters.

Property	Maximum value (typical value)
major radius (R_0)	1.75 *m*
minor radius (a)	0.47 *m*
plasma shape (δ,κ)	1.0 , 1.0 (i.e. circular cross section)
toroidal magnetic field (B_T)	3.0 *T* (2.25 *T*)
plasma current (I_p)	0.80 *MA* (0.40 *MA*)
pulse length	10 *s* (6 *s*)
Ohmic power (P_{Ohmic})	(0.3 *MW*)
NBI power (P_{NBI})	2 × 1.5 *MW* (co- and counter injection)
ECRH power (P_{ECRH})	0.8 *MW* (at 140 *GHz*) 0.3 *MW* (at 110 *GHz*)
ICRH power (P_{ICRH})	2 × 2.0 *MW* (at 25 - 38 *MHz*)
central ion temperature (T_i)	(1.0 *keV*)
central electron temperature (T_e)	(1.0 *keV*)
central electron density (n_e)	($3.0\cdot10^{19}$ m^{-3})

TEXTOR is a limiter tokamak, with its inner wall equipped with three different limiter types. First of all, the main limiters are placed at certain toroidal positions (on the top, bottom, and low-field side) and can be moved in- and outwards poloidally for shaping the plasma and testing materials. The second limiter is a full toroidal bumper limiter, which consists of carbon tiles covering about one-third of the poloidal circumferences at the high-field side. Its function is twofold: it allows for the plasma to be positioned close to the high-field side, protecting the inner wall from the deposited energy fluxes in a disruption. During application of the perturbation field from the DED (see section 3.1.3), it also serves as a divertor target. Thirdly, TEXTOR is provided with a full toroidal belt limiter located on the low-field side at about 45 degrees below the equatorial plane. This Advanced Limiter Test II (ALT-II) is designed to deal with the full heat load of the plasma (8 *MW*) for up to 10 *s*, and is equipped with turbomolecular pumps to obtain particle removal for all gases [26].

Apart from Ohmic heating of about 0.3 *MW* via the induced current I_p, the plasmas in TEXTOR can be heated in three additional ways: by Ion Cyclotron Resonance Heating (ICRH), by Electron Cyclotron Resonance Heating (ECRH), and by Neutral Beam Injection (NBI). The first heating method, ICRH, is based on power absorption by ions that are gyrating around magnetic field lines with a cyclotron frequency equal to the angular frequency of the electric field of injected microwave radiation. At TEXTOR, there are two ICRH systems each capable of injecting a power of 2 *MW* using waves with a frequency of 25 - 38 *MHz* [27].

The principle of ECRH is the same as that of ICRH, but in this case the power is absorbed by electrons at the second harmonic of their cyclotron resonance frequency. TEXTOR has two gyrotrons installed for injecting EM-waves in the extra-ordinary polarisation mode [28]. The 110 *GHz* gyrotron has a maximum power of 0.3 *MW* and pulse length of 0.2 *s*; the 140 *GHz* gyrotron can be operated at maximum values of 0.8 *MW* and 10 *s*. At these high frequencies, the corresponding wavelengths are short (*mm* range) allowing for narrow power deposition profiles, contrary to what can be achieved by ICRH. Using a moveable front mirror, ± 25° elevation (vertical) and ± 45° rotation (horizontal), the angle of injection can be varied which enables accurate positioning of the heating power. Exploiting these possibilities, experiments can, for example, be carried out investigating the effects of Electron Cyclotron Current Drive (ECCD) and heating inside magnetic islands [29].

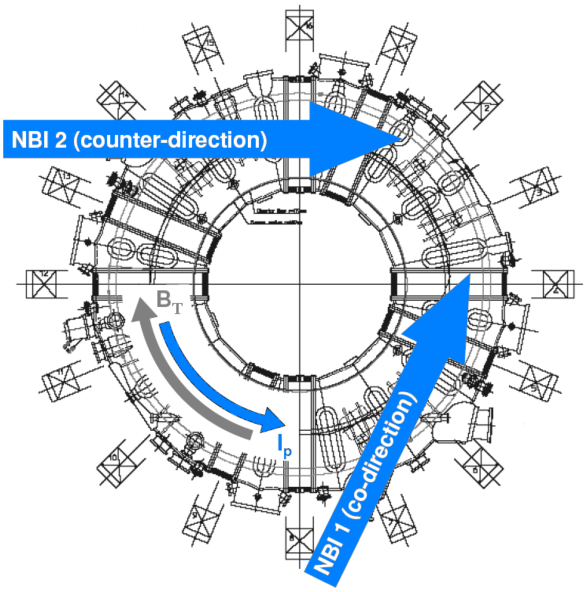

Figure 3.1 : *Top-view of the TEXTOR tokamak, with the 16 toroidal field coils, showing the co- and counter-directions of the neutral beams, and the standard plasma current* I_p *and toroidal magnetic field* B_T.

The two neutral beam injectors shown in Figure 3.1 are the third source available at TEXTOR for plasma heating. For the experiments described in Chapter 4 and Chapter 5 only the NBI 1 is used, since that is the one observed by the CXRS viewing geometry at TEXTOR. The direction along which the highly energetic neutral particles are injected is tangential in order to obtain a long absorption path. The NBI 1 is aligned in the same (i.e. co-) direction as the plasma current I_p, and NBI 2 has an opposite (i.e. counter-) direction. Through charge exchange reactions with the bulk plasma ions (cf. (2.17)), the neutral beam particles become ionised as well, and consequently transfer their energy and momentum to the plasma in further collisions. Each injector is, at maximum, capable of coupling 1.5 *MW* into the plasma for up to 10 *s* [30], injecting particles with an energy of 55 *keV/amu* (this is in the range of the maximum effective emission-rates for CX reactions, see Figure 2.6 and [16]).

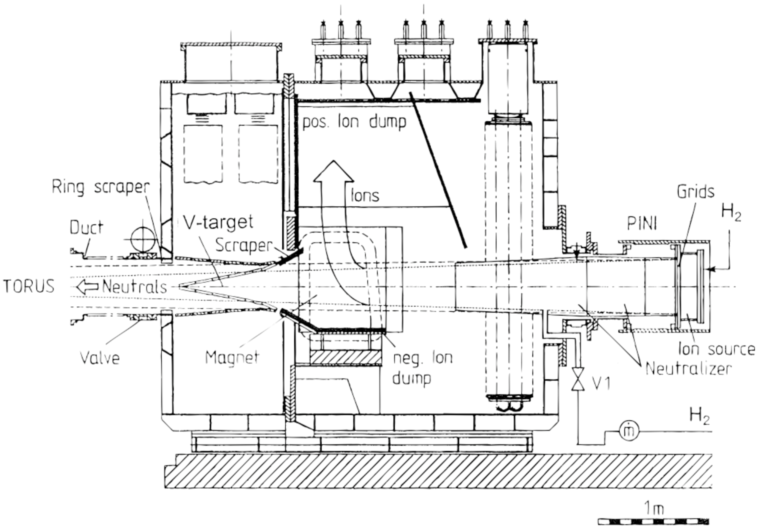

Figure 3.2 : *Scheme of the neutral beam injection system at TEXTOR. The main elements are the ion source, followed by the acceleration grid, the neutralizer cells, the deflection magnet and its ion dumps, the box scrapers, and the V-target (annex calorimeter).*

The neutral beams are produced by first ionizing the gas (usually H_2, but also D_2 and *He* are available), which is then accelerated in a grid system and neutralized again for about 50 % in a gas target neutralizer. Next, the remaining positive and negative ions are deflected towards an ion dump by a magnet, and the neutral beam particles pass the V-target to enter the plasma. The V-target acts as an aperture stop, which regulates the injected power by adjusting the vertical beam profile (at open V-target, the beam has a FWHM of 20 cm). During simultaneous operation of the two beams, the toroidal momentum input can be balanced which determines the net plasma rotation. Since the momentum transfer to bulk ions and electrons is in general not the same, tangential beam injection drives current as well.

3.1.2 Utilized plasma diagnostics

Apart from the charge exchange diagnostic, which is extensively described by the theory in paragraph 2.2 and the technical implementation in paragraph 3.2, there are about 50 other diagnostic systems available at TEXTOR [31]. The most basic ones, used for the experiments described in Chapter 4 and Chapter 5, are described here in some more detail. They namely are the techniques of laser interferometry (for determining the electron density, cf. (2.25)) and Electron Cyclotron Emission (ECE, for comparing electron and ion temperatures).

The electron density (n_e) can be measured using interferometry, where the phase velocity of a laser beam going through the plasma is compared to that of a reference beam. The phase difference depends on the refractive index of the medium, which on its turn is related to the (average) electron density. At TEXTOR, there is a far-infrared (336.6 μm)HCN laser available which intersects with the plasma at nine different radial positions. Via Abel-inversion the line-integrated electron density measurements are converted into electron density profiles $n_e(r,t)$ with an estimated error of about 5%. With a time resolution of 20 kHz, the line-integrated density signals are used for real-time density and position control.

Measurement of the electron temperature T_e is based on the electron gyration movement around magnetic field lines. The radiation emitted at the electron cyclotron frequency can be regarded as black-body radiation, because for usual densities the plasma is optically thick at this frequency. Applying the Raleigh-Jeans approximation of Planck's law, the intensity of ECE can be related to the temperature. Since the frequency of ECE is proportional to the local magnetic field $B(R)$ (via $\omega_e = e{\cdot}B(R)/m_e = e{\cdot}B_0R_0/m_eR$), local electron temperatures $T_e(R)$ can be derived from ECE intensities as a function of their frequency. An intensity calibration of the microwave detectors is necessary though, which is usually done with a 'hot' source or by cross-calibration on e.g. the Thomson scattering diagnostic. At TEXTOR, there is an 11-channel, fixed frequency system available (EC11), which allows for temperature profile measurements $T_e(R,t)$ with a sampling rate up to 10 kHz. The fixed frequencies of the EC11 system are in the range of 105 - 145 GHz, which corresponds to a region of R = 1.55 - 2.14 m in case of a typical toroidal magnetic field of B_T = 2.25 T. A second system, that of ECE-Imaging, can provide two-dimensional T_e profiles measured by 16 detector elements, each split up in 8 frequency bands, which corresponds to an area of approximately 8 × 16 cm.

A system that is capable of measuring both electron density and temperature profiles simultaneously is that of Thomson scattering. It is based on the scattering on free electrons of the light from an intra-cavity ruby laser, vertically shot through the plasma. For a Maxwellian velocity distribution of the electrons, the measured spectrum has a Gaussian shape; where the Doppler shift relative to the laser wavelength is a measure for the velocity of the electrons, the intensity of the spectrum is a measure for the electron density (but it requires an absolute calibration), and its width is related to the electron temperature. At TEXTOR, the laser chord going through the plasma has a horizontal offset of 9 cm from the tokamak centre, and measurements can be performed in either core or edge mode. For core measurements, the full 90 cm laser chord is imaged on the 120 channels of the spectrometer, resulting in a resolution of 7.5 mm. In edge mode, the upper 16 cm of the chord are imaged on 98 channels so then the diagnostic has a spatial resolution of 1.7 mm. The system is designed for measuring up to 3 laser bursts of 5 to 10 ms with a time resolution of 10 kHz, each burst consisting of 40 laser pulses of 15 J. However, since the time-scales of the conducted experiments are much longer, the Thomson scattering diagnostic has not been used for the work described in this thesis.

3.1.3 The Dynamic Ergodic Divertor

As already shortly introduced in 3.1.1, TEXTOR is equipped with a unique tool for applying a magnetic perturbation field to the existing helical field [32]. The Dynamic Ergodic Divertor (DED) consists of a set of 16 helical coils located at the high-field side, as shown in Figure 3.3, behind the carbon bumper limiter which acts as a divertor target plate during operation. Making one toroidal turn from top to bottom, the coils are aligned to the q = 3 magnetic field lines. Two compensation coils are added (above and below) to reduce the stray fields.

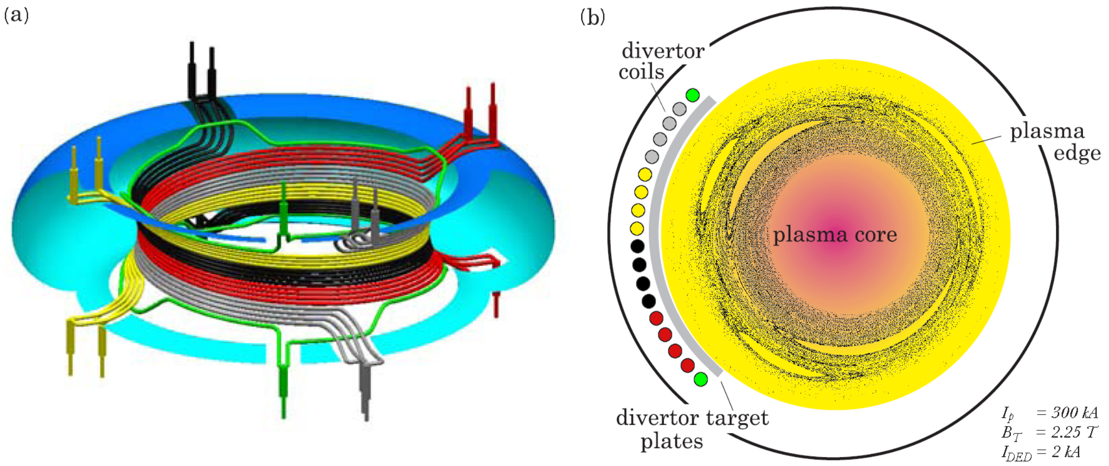

Figure 3.3 : *DED coil configuration installed in the 3/1 mode at the high-field side of the TEXTOR vacuum vessel. The four groups of differently phased (grey, yellow, black, and red) coil currents plus the two compensation coils (green) are shown in (a). The resulting vacuum field is shown as a Poincaré-plot in (b)* [34].

The main use of the DED is found in research of plasma edge physics (e.g. in studying transport and heat load distribution on the carbon tiles, [33]) and that of suppressing instabilities ([15], [29]). The reason for this is that it generates a perturbative magnetic field when a current is applied to the coils. In the 3/1 coil configuration, shown in Figure 3.3a, there is a phase shift of 90° for the current of the next group (toroidally located 90° further on the vessel) and all coils in one group carry the same current. Calculating the superposition of the perturbation field on the existing TEXTOR magnetic field [34] provides a vacuum magnetic field structure, which visualises the effect of the perturbation; however, it does not take the reaction of a plasma into account. In Figure 3.3b, such a vacuum magnetic field calculation (for $I_p = 300\ kA$, $B_T = 2.25\ T$, and $I_{DED} = 2\ kA$) is shown as a Poincaré plot for a full poloidal cross section. In this representation, one magnetic field line is followed many toroidal turns and leaves a mark every time it crosses this section.

Apart from the $m/n = 3/1$ and $m/n = 2/1$ vacuum islands that can clearly be seen in the Poincaré plot (where m and n denote the poloidal and toroidal mode numbers), there are also three zones in the plasma induced by the DED. The first zone, nearest to the edge, is the so-called laminar zone where magnetic field lines connect to the wall after just a small number of toroidal turns (leaving only a few marks in the Poincaré plot). In the second zone, the field lines fill up a volume and show chaotic behaviour due to the presence of (overlapping) magnetic islands, hence this is referred to as the ergodic or stochastic zone. In this region, increasing the DED current I_{DED} leads to growing magnetic islands and increased ergodic behaviour. The third zone is the regular zone, where the influence of the DED has drastically been reduced (as it decreases with r^m) and the field lines form circular flux surfaces again.

The DED is capable of being operated with both AC and DC currents. In DC mode, the resulting perturbation field is static, whereas it rotates during AC operation. The direction of the rotation depends on whether AC^+ or AC^- is used; in AC^+ the perturbation field rotates toroidally clockwise (as seen from the top, see Figure 3.1) and poloidally from top to bottom at the high-field side (cf. Figure 3.3b), in AC^- both directions are reversed [15]. In addition to the 3/1 mode it is also possible to operate the DED in 12/4 or 6/2 mode, in which its influence is significantly different and more localized to the edge. For the conducted experiments, however, the DED has been used in the above described 3/1 configuration, with AC^- currents at a frequency of 1 kHz up to a maximum of 2 kA.

3.2 CXRS diagnostics

In this paragraph, a detailed description is given of the implementation of the CXRS diagnostics, for which the theoretical aspects have already been introduced in paragraph 2.2. The first section explicates the different viewing geometries used in TEXTOR; the spectrometers that analyse the observed CX emission are described in the second section.

3.2.1 Equatorial lines-of-sight and the top-view ITER-pilot system

Similar to the one line-of-sight that has been used in Figure 2.5 to describe observation of CX emission, TEXTOR is equipped with three CXRS systems as can be seen in Figure 3.4a. All three systems are viewing the NBI 1 in the equatorial plane, and have their lines-of-sight directed tangentially to flux surfaces. Two systems, the core and edge lines-of-sight, are viewing towards the direction of the NBI 1; the third (MSE) system observes from the other side of the beam, along with the injected neutrals. The neutral beam is indicated by its FWHM of about 20 *cm*.

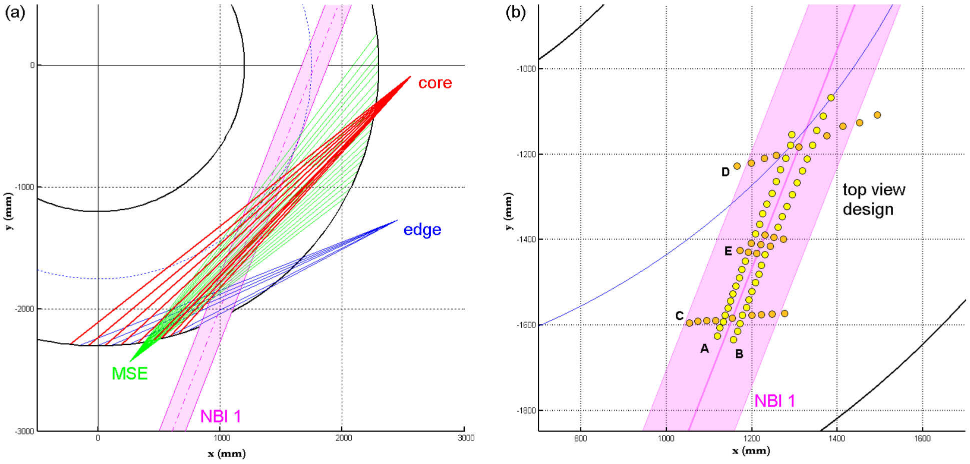

Figure 3.4 : *An overview of the three CX observation systems at TEXTOR is shown in (a): the core, edge, and MSE system in respectively red, blue and green lines-of-sight. Figure (b) shows the intersection pattern of the top view lines-of-sight and the neutral beam.*

As part of this work, a fourth system has been installed which mimics the top view design that will be used in the future ITER tokamak [35]. Its intersection pattern with NBI 1 is shown in Figure 3.4b and displays five sets of lines-of-sight, 71 in total. Two sets of 22 lines-of-sight are directed parallel to the path of NBI 1 (A and B; for beam attenuation measurements), two sets of nine across the neutral beam (C and D; for determining its width), and a set of nine (E) to be used as one spot.

Similar to the MSE setup, the top view design has its lines-of-sight directed along the injection of the neutral beam. The major advantage of this is that the radial variation of flux surfaces crossed during the intersection with the beam is small (compared to the lines-of-sight viewing towards the beam). Each flux surface yields the local physical properties of density and temperature, and the observed CX emission is the integrated sum along the line-of-sight of all the light emitted locally on a flux surface (cf. (2.23)). Hence, the integration over a small region of flux surfaces will result in a good radial resolution.

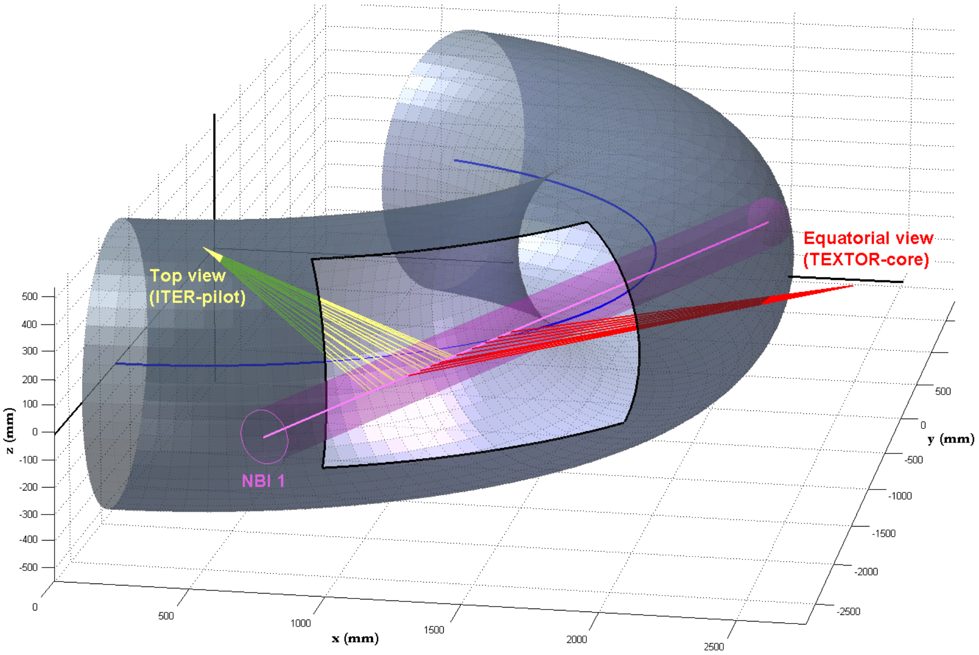
Top view
(ITER-pilot)
Equatorial view
(TEXTOR-core)
NBI 1
z (mm)
500
400
300
200
100
0
-100
-200
-300
-400
-500
x (mm)
0
500
1000
1500
2000
2500
y (mm)
500
0
-500
-1000
-1500
-2000
-2500

Figure 3.5 : *Three-dimensional cutaway view of TEXTOR and the neutral beam. Shown are all lines-of-sight of the equatorial (core) system and 18 observable ones of the new installed ITER-pilot system.*

A cutaway section of TEXTOR is shown in Figure 3.5, with all lines-of-sight of the core-CXRS system and 18 observable ones of the installed ITER-pilot system. Due to a changeover from prism to mirror (to bend the lines-of-sight towards the beam) during the installation of the top view system [36], the position of the designed intersection pattern from Figure 3.4b has shifted outwards. Contrary to the pattern of Figure 3.4b, which has been determined from in-vessel measurements during a shutdown period, the position of the lines-of-sight shown in Figure 3.5 is derived from BES measurements [37] (see section 2.2.3).

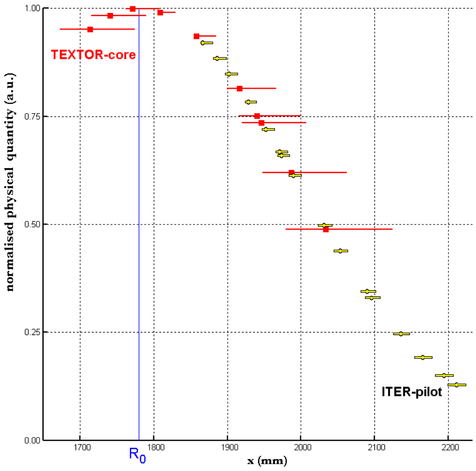

Figure 3.6 : *Radial resolution of the top view and equatorial system on an arbitrary Gaussian profile. The differences between the two systems result from their position relative to NBI 1. It can also be seen that the ITER-pilot system does not have full coverage up to the centre of the plasma.*

The radial resolution of the lines-of-sight of the installed top view system is shown above in Figure 3.6, in comparison to the radial resolution of the TEXTOR-core system. As can be seen from this figure, the two systems are complementary with an overlap region in the middle, but the ITER-pilot system clearly has a better radial resolution. However the equatorial system has been used for the experiments described in Chapter 4 and Chapter 5, since they required core measurements of the helium density.

3.2.2 Spectrometer setups

The light collected by the observation systems near the plasma, is transmitted through a bundle of optical fibres to the spectrometers. In order to simultaneously gather spectra from both helium CX- and beam emission, two spectrometers (of the Pfund and Littrow type) are used in a setup as shown in Figure 3.7. The light coming from the plasma through an optical fibre is first collimated and then split by a beamsplitter. This directs the wavelength range around 468 *nm* (HeII-CX) towards the Pfund spectrometer and the range around 656 *nm* (BES) towards the Littrow spectrometer. The collimated beams are focussed again on the entrance slits, and then guided by one (or more) mirrors inside the spectrometers towards a parallel beam fully illuminating the gratings. The light reflected from the gratings then follows a reversed path that images it on a CCD camera. In Table 3.2, at the end of this section, a comprehensive list is given for the spectrometer and camera properties of the combined setup of Figure 3.7.

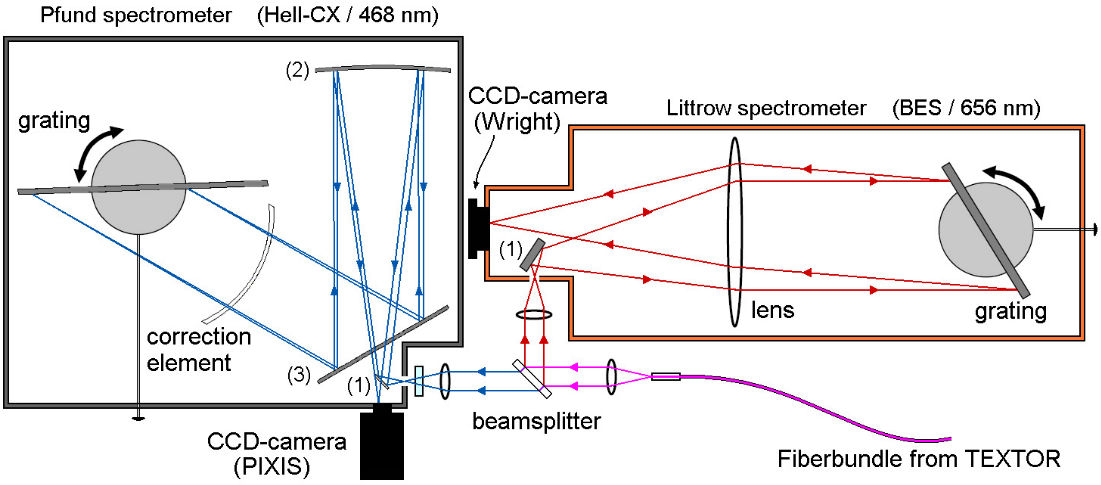

Figure 3.7 : *Spectrometer setup for simultaneous measurement of the helium CX- and beam emission. After collimating the light from the fibre bundle, it is split in two wavelength ranges and directed to the two spectrometers. The reflected light from the grating is then imaged onto a CCD camera.*

The wavelength of the light reflected on the grating, is dependent on the angle α of the grating, the observed order of reflection *m*, and the number of lines *d* on the grating:

$$m\lambda = d\sin(\alpha). \tag{3.1}$$

The dispersion at the image on the CCD camera, i.e. the spread of the wavelength along the size *x* of the chip, is given by

$$\frac{\mathrm{d}\lambda}{\mathrm{d}x} = \frac{1}{mfd}\sqrt{1-\left(\frac{m\lambda d}{2}\right)^2}, \tag{3.2}$$

where *f* is the focal length to the CCD chip. For the Littrow spectrometer this distance is from the lens to the camera, for the Pfund spectrometer from mirror (2) to the camera [38].

There are two different cameras attached to the spectrometers; the Wright camera on the Littrow spectrometer has a chip of 1152 × 298 pixels, with each pixel being 22.5 × 22.5 *μm*. The short side of the chip is placed in the wavelength direction, and the long side is used to project multiple fibre images onto (it is divided in two halfs, one is continuously illuminated and the other is used for fast transfer of captured images). With a focal distance of f = 750 *mm*, a grating of 1200 *grooves/mm*, and observing a wavelength of 656 *nm* in the first reflected order, the dispersion of the Littrow system is $2.4\cdot10^{-2}$ *nm/pixel*. The PIXIS camera on the Pfund spectrometer has a chip of 1340 × 400 pixels, with each pixel being 20 × 20 *μm* and the long side in the wavelength direction. With a focal distance of f = 480 *mm*, a grating of 200 *grooves/mm*, and observing a wavelength of 468 *nm* in the 19th reflected order, the dispersion of the Pfund system is $0.5\cdot10^{-2}$ *nm/pixel*. In order to take synchronized measurements, a shutter has been placed between the fibre bundle and the collimating lens. While the Wright camera is able to perform faster (at 30 *ms*), it is limited by the PIXIS camera which has a read-out time of 40 *ms*, since that controls the shutter.

Although the method of combined measurement of the intensities of HeII-CX and BES does not require an absolute calibration (as explained in section 2.2.3), the Pfund spectrometer has been absolutely calibrated in order to use its HeII-CX measurement in a code that calculates the neutral beam density (see section 4.2.2). The total throughput is given by the photon transmission times the étendue of the system. Using an integrating sphere (i.e. a light source that homogeneously emits a known amount of photons per wavelength), the transmission through the lenses plus spectrometer was measured to be about 5 %. The systems étendue per fibre follows from

$$E = A\cdot\Omega = \frac{\pi d_{fib}^2}{4}\cdot\int_0^{2\pi} \mathrm{d}r' \int_0^{\vartheta_{\max}} \mathrm{d}\cos(\vartheta) = \frac{\pi d_{fib}^2}{4}\cdot 2\pi\left(1-\sqrt{1-\left(\frac{1}{2F}\right)^2}\right), \qquad (3.3)$$

where A is the area of the image of the fibre at the spectrometers entrance slit, and Ω the solid angle of its illumination. The image area is equal to the fibres cross section divided by two times the demagnification. The angle $\vartheta_{\max}$ is determined by the numerical aperture and can be expressed in terms of the spectrometers F-number (relative aperture). The results of the absolute calibration are listed in Table 3.2.

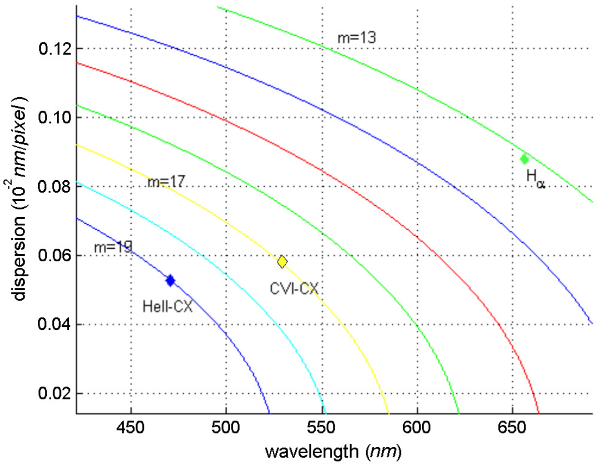

Figure 3.8 : *Wavelength dependence of the dispersion (3.2) for the observed reflection orders m = 13-19 for the combination of Pfund spectrometer and PIXIS camera. Although the dispersion for HeII-CX seems nearly linear from 450 - 500 nm, it was found to be so only in a small region around 468 nm.*

Although a pixel-to-wavelength conversion can be done using (3.1) and (3.2), as can be seen in Figure 3.8, a consistency check has been performed for the new installed Pfund spectrometer using calibration lamps with a cold emission at known wavelengths (from the NIST database [17]). However, for the combination of the Pfund spectrometer and PIXIS camera, the dispersion on the CCD-chip did not show a linear dependence on the wavelength. This non-linear dispersion excludes the third option commonly exploited for pixel-to-wavelength conversion, namely the use of known emission lines from the plasma itself (cold reference lines that are useful in the analysis of the recorded spectra, or impurity lines that light up during a disruption, see paragraph 4.1). The dispersion is linear, though, in a small wavelength region around the HeII-CX emission at 468 *nm*, so a suitable pixel-to-wavelength calibration can still be performed.

Last important point concerning the use of a spectrometer is its instrument function, a convolution of the Gaussians of the observed spectral lines and the response function of the instrument. The width of the instrument function is strongly determined by the width of the entrance slit, where a narrow slit width results in a narrow instrument function, but at the same time reduces the measured intensity. Therefore, it is chosen to be equal to the width of the focussed fibre image, which results in an instrument function that corresponds to a temperature of 18 *eV*.

Table 3.2 : Properties of the spectrometers and cameras.

Setup	He-II CX	BES
spectrometer	Pfund	Littrow
relative aperture (*F* /#)	3.0	4.5
focal length (*f*)	480 *mm*	750 *mm*
étendue (*E*)	$6.2\cdot10^{-9}$ m^2 sr·(per fibre!)	$2\cdot10^{-9}$ m^{2}sr
transmission	5 %	-
grating	Echelle (200 grooves/*mm*)	ruled (1200 grooves/*mm*)
wavelength vicinity	468 *nm*	656 *nm*
order (#)	19	-1
dispersion	2.59 *Å/mm*	10.2 *Å/mm*
CCD-camera	PIXIS	Wright
read out (max. speed)	full frame (40 *ms*)	frame transfer (30 *ms*)
chip size (pixels)	1340 × 400	298 × 1152
pixel size	20 × 20 *μm*	22.5 × 22.5 *μm*
quantum efficiency (*Q.E.*)	89 %	40 %

Chapter 4

Helium spectral analysis

Using the CXRS viewing lines in the equatorial plane, see section 3.2.1, experiments have been performed using the (ITER-pilot) échelle spectrometer in order to determine helium concentrations. This chapter describes the steps of the analysis that lead to a helium density profile as a function of space and time.

In the first paragraph the spectrum as it is recorded by the CCD-camera will be considered. Its most distinct features are described and it will be shown how to derive the helium ion temperature from this spectrum. In the second paragraph the intensity, which is derived from the same spectrum, will be used to obtain a helium density profile. This method of acquiring a density profile is then also compared to two other types of density measurements.

4.1 Characteristics of the helium spectrum

Typical spectra that are recorded with the CCD-camera on the échelle spectrometer, look like the ones shown in Figure 4.1. The intensity differences are due to switching the NBI on and off, and the amount of helium in the plasma. At first sight the spectrum seems to consist of four main lines. The identification of the origin of these lines has already been described extensively in literature, e.g. [16], [18], and [39].

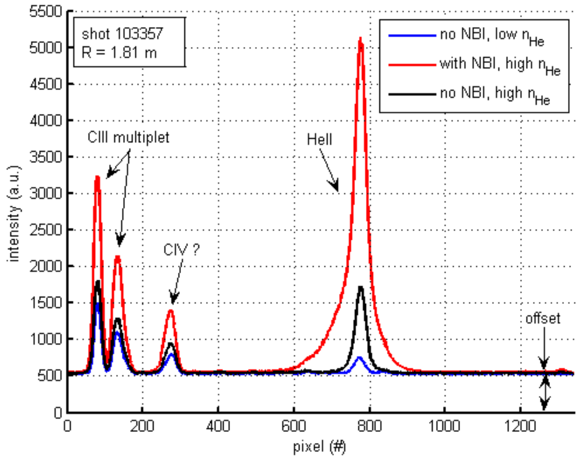

Figure 4.1 : *Typical helium spectra recorded in the CXRS equatorial setup, with the PIXIS CCD-camera on the Echelle spectrometer; The three different measurements represent common plasma conditions.*

The first two intense lines on the left side of the spectrum are attributed to CIII emission from the edge. This CIII-multiplet is represented by emissions at $\lambda_{1,2,3}$ = 4647.42, 4650.18, and 4651.37 $\AA$ with amplitude ratios of 5:3:1; note that the first two lines actually represent three CIII emission lines. The distinct line on the right side of the spectrum is mainly attributed to the $n = 4 \rightarrow 3$ transition of HeII, emitting at 4685.25 $\AA$. Its characteristics will be in detail discussed further on in this paragraph.

However, regarding the smallest of the main four lines (third from the left), in this work a remarkable difference from the identification in [18] (and [16], [39]) is presented for the first time. In all the other representations this line is identified as BeIV ($n = 6 \rightarrow 5$ transition, emitting at 4658.5 Å), as it is recognized as an impurity resulting from the beryllium wall in those cases. In TEXTOR though, the wall is not made of beryllium, so it is impossible that this third line originates from BeIV. Consulting the NIST Atomic Spectra Database [17], there are several other possibilities for this line. The most plausible candidates are CIV emission at 4658.30 Å, CIII at 4659.06 and 4665.86 Å, and OII at 4661.63 Å. There are also possibilities for N, Ne, and Fe, but these elements are usually not abundantly present in the plasma. It might be useful to investigate whether or not the identification of this line as a BeIV line is in fact correctly described in literature and which of the other possibilities is the one observed here. An accurate identification is, however, not relevant for the work described in this thesis.

The pixel to wavelength conversion that was done in order to calibrate the spectrometer (see section 3.2.2) can not be performed during or after every shot. It would therefore be helpful to find a reference line originating from the plasma, preferably a small but intense plasma edge line. Edge lines are the preferable choice, since it automatically results in a fixed position. This is because it is assumed that particles at the edge hardly rotate as a bulk (they do move a lot of course) and therefore have almost no Doppler-shift in their emission. Considering the fact that the dispersion is not linear over the chip, as was already mentioned in section 3.2.2, none of the three lines on the left can be used for this purpose.

But, a pixel to wavelength conversion can still be performed assuming linear dispersion around the middle of the CCD-chip, and discarding all lines at the edges. Zooming in to the wavelength vicinity of 4680 Å in this way also reveals more characteristics of the HeII spectrum. Especially during a disruption, when all energy in the plasma is suddenly lost, all impurities light up with cold intense emission lines as is shown below in Figure 4.2. In the surrounding area of HeII there are at least four impurity lines emerging, but they are not always clearly visible during normal plasma conditions. Therefore, the cold but intense HeII edge line at 4685.71 Å is chosen as a reference line, since that one as a rule appears prominent in all helium spectra (cf. Figure 4.1).

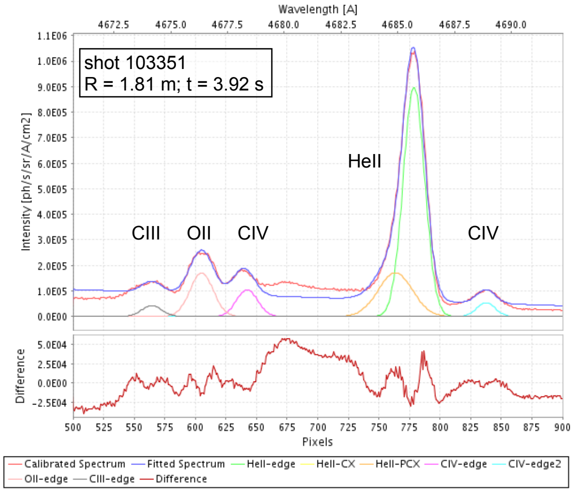

Figure 4.2 : *Spectrum recorded during a disruption, which reveals detailed characteristics of the region around 4686 Å. The HeII edge line is chosen as a reference line, and there are indications for the origin of the four clearly visible impurity lines. It seems very likely that at least one more emission line is present at 4680 Å.*

In [17] and [40] some indications have been found for the four impurity lines surrounding the HeII reference line in Figure 4.2. In order to be able to account for these lines in fitting the spectrum, they are dealt with as edge lines with wavelengths of $\lambda_{1,2,3,4}$ = 4678.20, 4688.70, 4676.24, 4673.95 $\AA$. The $\lambda_{1,2}$ lines most likely originate from CIV $n = 6 \rightarrow 8$ and $n = 7 \rightarrow 11$ transitions respectively, and appear to have the same temperatures and amplitudes. They also seem to experience similar rotation relative to the HeII edge line and their wavelength difference is therefore fixed; note that, strictly, their rotation suggests they are not edge lines. From [17] it is alleged that λ_3 originates from OII emission. The λ_4 line may be attributed to a CIV transition, and it seems likely that at least one more emission line is present in the vicinity of 4680 $\AA$ but no clues have been found for its origin.

The spectrum recorded during the disruption, Figure 4.2, is also used for determining the instrument function of the spectrometer, which is used in the temperature calculation (see section 3.2.2). From the FWHM of 17.5 pixels of the cold HeII edge line, and the spectrometers dispersion of $5.39 \cdot 10^{-2}$ $\AA$/pixel determined in section 3.2.2, it follows for the instrument function σ that:

$$\sigma = \frac{FWHM_{HeII-edge} \cdot \frac{\mathrm{d}\lambda}{\mathrm{d}x}}{2\sqrt{2\ln(2)}} \approx 0.4\,\AA\,. \qquad (4.1)$$

With a pixel length of 20 μm, the FWHM of 17.5 pixels corresponds to 350 μm. The slit width has been set to 0.3 *mm* (demagnification of the lenses multiplied with the diameter of the fibres), which is then slightly too small. However, negative effects, such as a too low signal, have not been observed.

Before the final fitting procedure using KS4FIT can be started, the offset from Figure 4.1 has to be taken into account. It consists of two components; first there is the so-called dark current. It is determined from the signal recorded after a plasma shot, and has to be subtracted from all recorded spectra. The remaining baseline intensities can then be attributed to Bremsstrahlung emission. Due to an instrumental artefact however, the background shows a slope (e.g. seen in Figure 4.2), but this can be corrected for in KS4FIT. The importance of an accurate treatment of the background intensity will become clear in the next paragraph, because there Bremsstrahlung emission is used for calibration purposes.

When the pixel to wavelength calibration has been done (with the HeII edge line as a reference line), the impurity lines have been identified, the instrument function has been calculated, and the background has been treated correctly, what remains is the spectrum shown in Figure 4.3. The cold HeII line, already introduced above, originates from the cool plasma edge region where the emission is mostly due to electron impact excitation. The second source of HeII emission that has to be taken into account is the so-called passive emission. It stems from an intermediate layer between the outermost plasma edge and the separatrix, where charge exchange excitation can occur due to collisions with neutral hydrogen atoms that come from the wall. Since the plasma core mainly consists of fully stripped ions, no line radiation is expected from there, unless of course the neutral beam injection is switched on. Then high energy neutral particles penetrate into the core and cause charge exchange recombination reactions there. The observed HeII emission coming from the plasma core is then the so-called active charge exchange line. These three types of HeII emission have been described already in [18], where also a fourth source is mentioned. That is the so-called helium 'plume' emission, which results from a secondary excitation by electron impact of an ion that had already undergone a charge exchange reaction. Although 'plume' emission is calculated to be part of the helium spectrum (as a wide but low peak), it could not be identified in the spectra measured for this work.

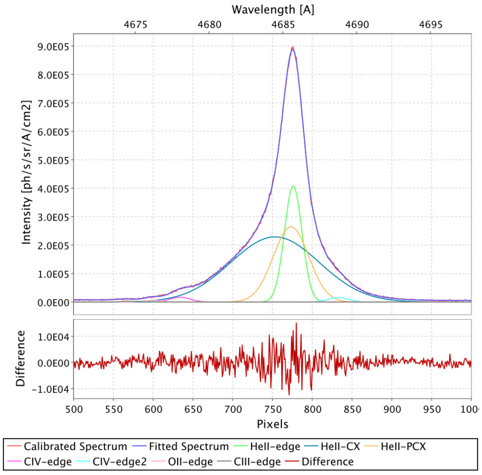

Figure 4.3 : *Definite fit of the HeII spectrum with up to 7 distinguishable lines. The most important of these is the active HeII-CX line from which the helium density and temperature can be derived.*

In the spectrum of Figure 4.3 the three types of helium CX emission are clearly recognized; whereas in Figure 4.2, logically, only the HeII-edge and a little passive helium CX emission are observed. It also becomes clear from Figure 4.3 that it is important to correctly take the impurities into account. If they would have been neglected, it would be rather easy to mistakenly find a much broader Gaussian to fit the HeII active CX line. According to (2.22) that would lead to a much higher temperature measurement.

In order to evaluate the measured ion temperatures from active HeII CX, Figure 4.4 shows them together with the electron temperatures that are routinely measured with ECE (which on its turn has been calibrated on Argon spectroscopy).

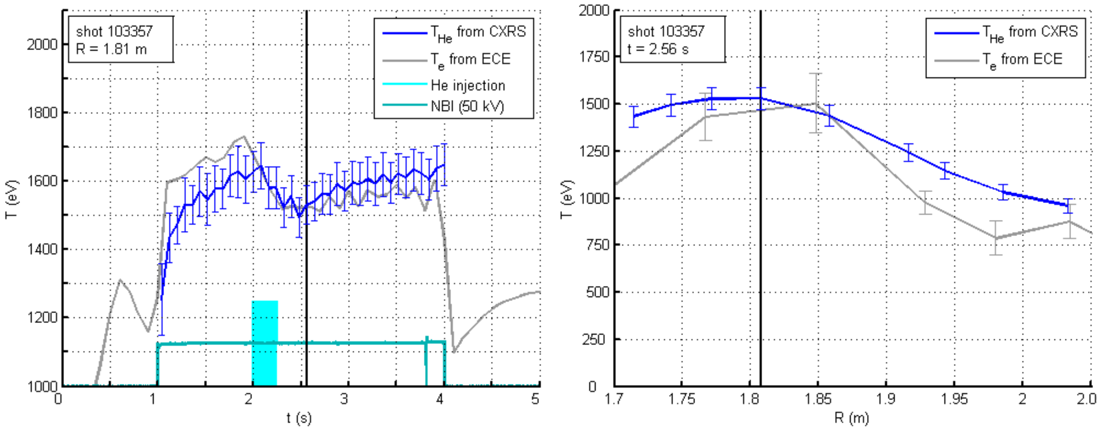

Figure 4.4 : *The helium ion temperature, determined from the width of the active HeII-CX line (shown in Figure 4.3) is compared to the electron temperature measured with ECE. In the left graph this is done for the measurements at R = 1.81 m; the right graph shows the measured temperature profiles at t = 2.56 s.*

As can be seen in the left graph of Figure 4.1, the ion and electron temperature differ somewhat prior to the helium injection at 2.0 *s*, which is due to the fact that they are governed by different collision time regimes. Afterwards, the density increase caused by the helium injection results in better consistency between ion and electron temperature. In the radial direction good agreement is observed near the plasma centre; towards the edge however, electron temperatures seem to be a bit lower than ion temperatures.

4.2 Measuring a density profile

In this paragraph the first question from paragraph 1.2 (*"What are the possibilities for measuring helium densities?"*) will be addressed. Three different ways for determining the helium concentration from measurements will therefore be compared to each other.

In the first section the helium concentration is derived from electron density measurements during an experiment with helium injection in the plasma. Section 4.2.2 contains the results from the 'CHarge Exchange Analysis Package' (CHEAP) [41], which incorporates calculations of the neutral beam attenuation. It uses those in resolving helium concentrations from intensity measurements of the active HeII-CX emission. Another way to derive helium concentration profiles from the same active HeII-CX intensities is to combine them with measurements of beam emission intensities. This approach, applying the method of combined CXRS and BES from section 2.2.3, is described in the third section.

4.2.1 Estimate by means of electron density

A quick method for calculating the concentration of helium in the plasma is looking at the electron density signal, which is readily available after each plasma shot. The electron density control system is set to maintain a specified value. When a vast amount of helium is then suddenly puffed in the plasma, increasing the electron density to a large degree, the control system will close all valves. Fully attributing the measured density increase to the helium injection, it is straightforward to determine from that the helium concentration.

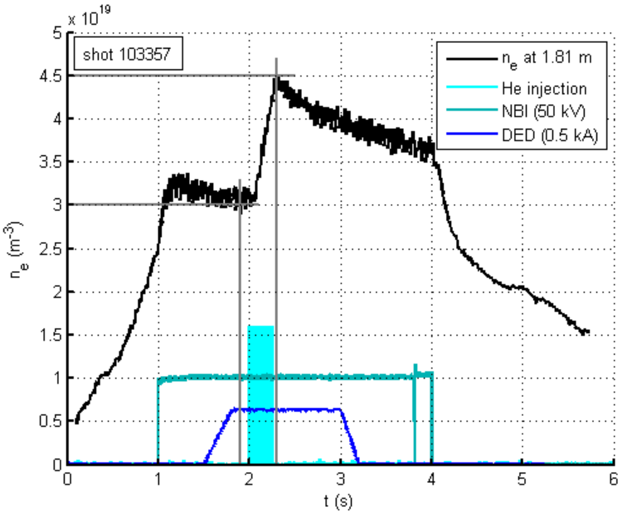

Figure 4.5 : *Electron density signal from the plasma centre (R = 1.81 m, where $\rho \approx 0.02$), measured with the interferometer. From the electron density increase around 2.0 s, due to the injection of helium, the helium concentration is measured to be (18 ± 3) %.*

Figure 4.5 shows the (Abel-inverted) electron density as a function of time for a central channel at radius 1.81 *m* in the experiment where helium is puffed in for 250 *ms* at 2.0 *s*. Ascribing the subsequent electron density increase to this injection of helium, it follows for the helium concentration that:

$$f_{He}(t_2) = \frac{\frac{1}{2}\left(n_e(t_2) - n_e(t_1)\right)}{n_e(t_2)} = 0.15 \pm 0.03 \,. \qquad (4.2)$$

However, in (4.2) it is assumed that there is no helium present in the plasma prior to the puff. Taking into account that the plasma does already contain some helium, (4.2) is adapted and becomes:

$$f_{He}(t_2) = f_{He}(t_1) \cdot \frac{n_e(t_1)}{n_e(t_2)} + \frac{\frac{1}{2}\Delta n_e}{n_e(t_2)} = 0.18 \pm 0.03 . \tag{4.3}$$

An estimate of 5 % helium (from the CXRS signal ratios) is used here for $f_{He}(t_1)$, and as a result the helium concentration is found to be (18 ± 3) %.

The measurement shown in Figure 4.5 is a typical example of the helium density and transport experiments that have been carried out, all of which at $I_p = 350$ *kA* and $B_t = 2.25$ *T*. The DED, in this particular experiment operated at 0.5 *kA*, is used in the transport experiments and its influence on helium will be considered in paragraph 5.2. Apart from the helium injection, the NBI is operated at full power (1.5 *MW*, at a beam energy of 50 *kV*) during all experiments. This gives the possibility to compare the above found result to density measurements based on the intensity of the active HeII-CX emission. In the next section this will be done with the charge exchange measurements that are evaluated using CHEAP.

4.2.2 Profile calculations performed with CHEAP

As has been shown in section 2.2.1, impurity concentrations can be derived from (2.25). However, the intensity of the active part of the charge exchange spectrum is proportional to the local neutral particle density in the beam as well. As the neutral particles from the NBI penetrate into the plasma, they get ionized and the local neutral density decreases. In [23] the theoretical modelling is described that forms the basis of CHEAPs numerical calculation of the beam attenuation; the main steps will be shortly discussed here as well.

Beam attenuation is caused by ionization of the neutral atoms that the beam injects in the plasma. The three important ionization reactions that are taken into account are electron collision impact, ion collision impact and charge exchange reactions with plasma ions. Defining S_1^{elec} and S_1^{ion} as the ionization rate coefficients from the zero density ground state due to respectively electron and ion impact, and defining the rate coefficient for charge exchange loss from the ground state as q_1^{CX}, the total ionization rate coefficient S_1 is given by

$$n_e S_1 = n_e S_1^{elec} + \sum_{ion} n_{ion} \left(S_1^{ion} + q_1^{CX} \right) . \tag{4.4}$$

From this it follows for the reduction of the ground state beam atom density n_1 that

$$\frac{\mathrm{d}n_1}{\mathrm{d}l} = -n_e \frac{S_1}{v_{beam}} n_1 . \tag{4.5}$$

In the calculation of the beam attenuation there are also extra sources of collisional losses, e.g. from the population of excited beam atoms. Their excitation and de-excitation electron and ion impact reaction rates have to be incorporated in (4.4) as well. The effective 'collisional-radiative' ionization coefficients that then replace S_1 are stored in the extensive look-up tables of the ADAS (Atomic Data and Analysis Structure) database [42] which CHEAP uses.

With an effective ionization rate S^{eff} for all processes associated with beam atoms of speed v_{beam}, and subsequently defining a stopping cross-section $\sigma^{eff} = S^{eff} / v_{beam}$, it easily follows from (4.5) that the neutral beam density n_{beam} is equal to:

$$n_{beam}(r) = n_{beam}(0) \cdot e^{-\int_0^r n_e \sigma^{eff} \, \mathrm{d}l} \quad . \tag{4.6}$$

In order to determine the stopping cross-sections, the look-up tables of the ADAS database [42] are searched through. The ionization rates are related to the physical quantities of temperature T, electron density n_e, and beam voltage V_{beam}. The beam voltage V_{beam} is required in order to determine the beam velocity. For n_e the same interferometer measurements from section 4.2.1 are utilized again, and since the ionization rate also depends on T_e, the ECE temperature measurements from paragraph 4.1 are also used as input. Furthermore, the iterative process that follows from (4.6) also requires the input of the densities of other impurities (e.g. carbon, argon, nitrogen, etc.), for which estimates can be used in the absence of direct measurements.

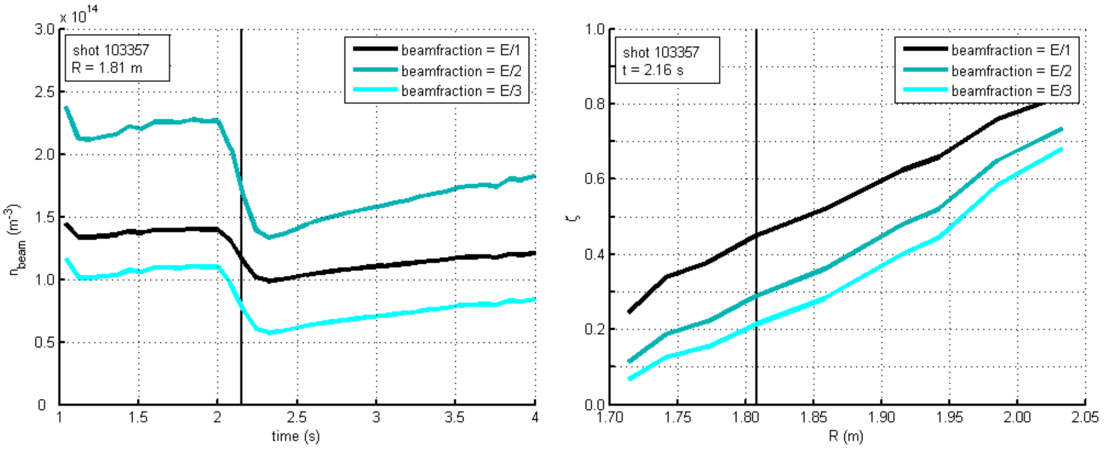

Figure 4.6 : *Result of the beam attenuation calculation by CHEAP for the centre of the plasma (R = 1.81 m). The beam density shown in the left graph and the beam attenuation (shown right) have been determined from these calculations for each of the three different beam fractions.*

Following this method, CHEAP is able to calculate the beam attenuation and density as is shown in the graphs of Figure 4.6. These calculations can then be extended in the iterative procedure to all the radii at which charge exchange intensities have been measured. With the input of electron density n_e, the helium charge exchange emission rate $q_{HeII\text{-}CX}$ also from [42], and the active HeII-CX intensities I_{He} (measured in paragraph 4.1) it is now possible to calculate the helium density profile according to (2.25). The result of the calculation performed in this way with CHEAP is shown in Figure 4.7. As will be discussed in more detail in 4.2.4, the CHEAP calculation has integrating errors along the injection trajectory of the neutral beam. The errors increase with increasing beam attenuation, which in this calculation results in an error of 40 % for the helium density around the plasma centre (R = 1.81 m).

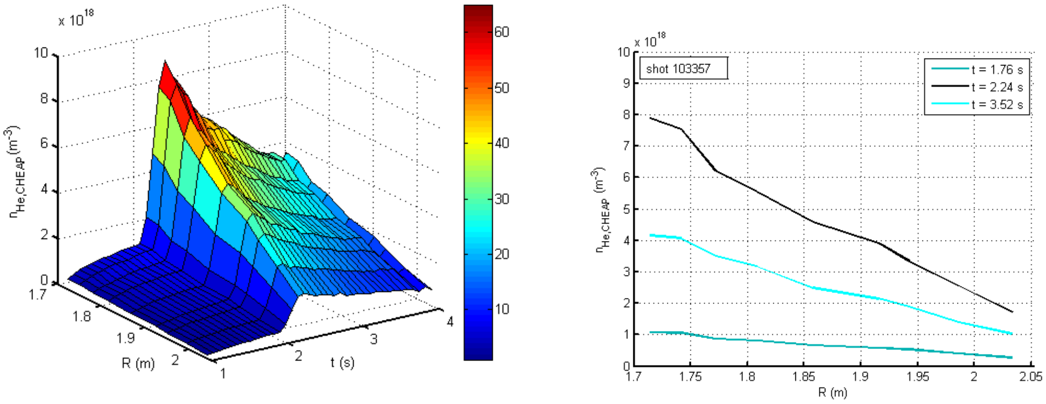

Figure 4.7 : *Calculation of the helium density profile with CHEAP, which is directly comparable to the measurement described in the next paragraph using BES intensities as a calibration.*

In order to compare CHEAPs helium densities to the method from section 4.2.1, the density in the centre (at R = 1.81 m) is recalculated to a helium concentration time-trace, as shown in Figure 4.8. As can be seen from this figure, the concentration in the centre, based on CHEAP, is about (14 ± 6) % shortly after the helium injection and from the measurement in section 4.2.1 it was found to be (18 ± 3) %. Apparently this method of using beam attenuation calculations slightly underestimates the helium concentration, at least in the centre. A comparison to the two other methods for the determination of helium concentrations will be done in section 4.2.4.

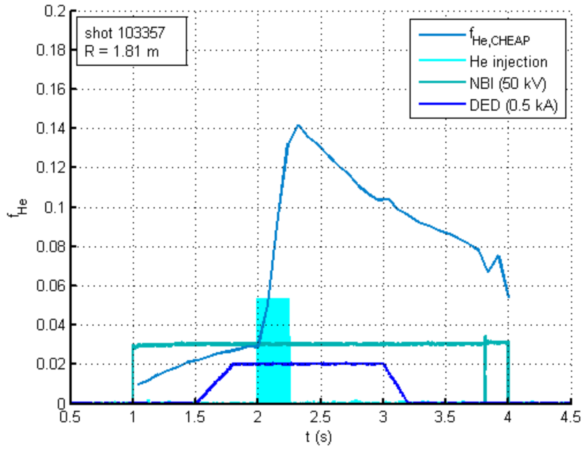

Figure 4.8 : *Helium concentration near the plasma centre, derived from a density profile based on the active He-CX intensities and beam attenuation calculations with CHEAP.*

In the next section a third method for determining the helium concentration is presented. There the attenuation calculation is bypassed by using beam emission spectroscopy as method for a relative calibration of the active HeII-CX intensities.

4.2.3 Using CXRS and BES for determining helium density profiles

As has been shown in the previous section, the helium concentration can be derived from the intensity of the active part of the charge exchange spectrum using (2.25). In this section the neutral particle density in the beam is coped with by using beam emission spectroscopy.

Simultaneous measurement of the intensity of the BES spectrum, along the same line of sight and with the same optics, can be used to exclude the difficulty of the beam density calculation and still provide a direct measurement of the helium concentration, as has already been described in section 2.2.3:

$$f_{He} = \frac{n_{He}}{n_e} = \frac{I_{HeII-CX}}{I_{BES}} \cdot \frac{q_{BES}}{q_{HeII-CX}} . \tag{4.7}$$

For the division of $I_{He,CXRS}$ by I_{BES} from (4.7), first the BES intensities have to be integrated over the three energy components that have been measured (as shown in the right graph of Figure 4.9). These represent the full, half, and one third energy of the neutral beam. Then, in order to do the division correctly, a relative calibration on the background intensity has to be done as well [39]. This is necessary because the Bremsstrahlung emission is dependent on the wavelength λ (2.26), which differs for the two measured spectra:

$$c = \frac{\lambda_{HeII-CX} \cdot I_{He,Brems}}{\lambda_{BES} \cdot I_{BES,Brems}} . \tag{4.8}$$

In the left graph of Figure 4.9 the intensity measurements of the active He-CX and BES are shown. These measurements have been performed on the same discharge as was used in the previous section, so the results can be compared in section 4.2.4.

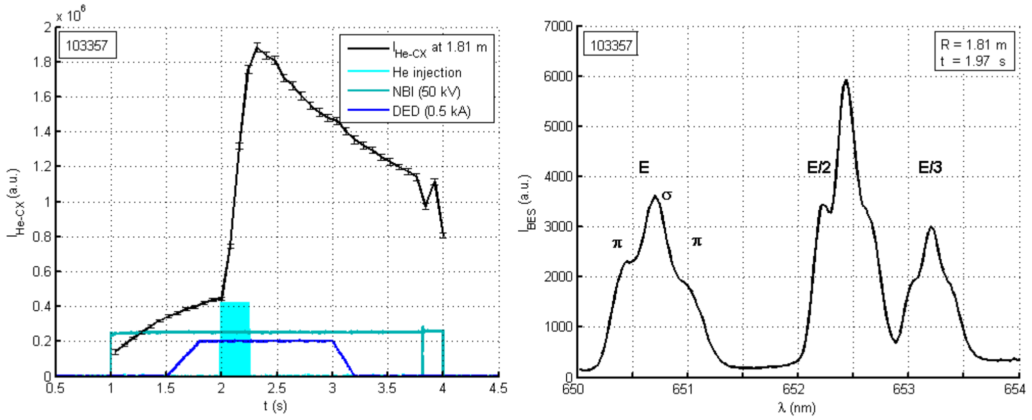

Figure 4.9 : *The intensity of the active HeII-CX line, during the shot with a helium puff at 2.0 s, is shown in the left graph. In the right graph the three components of the BES intensities are shown; based on these two measurements the helium concentration can be calculated.*

For the emission rates q_{BES} and $q_{HeII-CX}$ from (4.7) the look-up tables of the ADAS database [42] are accessed again. As $q_{HeII-CX}$ is dependent on T_i, the temperature determined from the active HeII-CX line has been used. This temperature measurement is the same as the one that has already been described in paragraph 4.1.

Now, combining the intensity measurements of the active HeII-CX and BES, and performing the relative calibration on Bremsstrahlung emission, the helium concentration is given by the modified equation (4.7) where *E/i* represent the three energy fractions in the neutral beam:

$$f_{He} = \frac{n_{He}}{n_e} = \frac{I_{HeII-CX}}{c \cdot \sum_{i=1,2,3} \left(I_{BES} \cdot \frac{q_{HeII-CX}}{q_{BES}} \right)_{E/i}} . \tag{4.9}$$

The result of the above described method is presented in Figure 4.10, where the helium concentration for the central channel (at radius 1.81 *m*) is shown as a function of time. The helium concentration after the injection at 2.0 *s* is measured to be (16 ± 5) %. The error margin of 30 % consists of two parts; about 6 % can be attributed to the measurement errors in n_e, $I_{HeII\text{-}CX}$, and I_{BES}, the other 24 % result from the uncertainties in the calibration factor in (4.9) and the ADAS values of q_{BES} and $q_{HeII\text{-}CX}$. Since the data is taken from the same experiment as described in section 4.2.1, it is directly comparable to the results derived from Figure 4.5. The first conclusion must be that this method for measuring helium concentrations is applicable, since its result is in the same ball park as calculated by the CHEAP code as well as within the (18 ± 3) % margin found in 4.2.1 from the electron density. A more extensive discussion on the comparison between the three measurement methods and on the error margins is found in the next section.

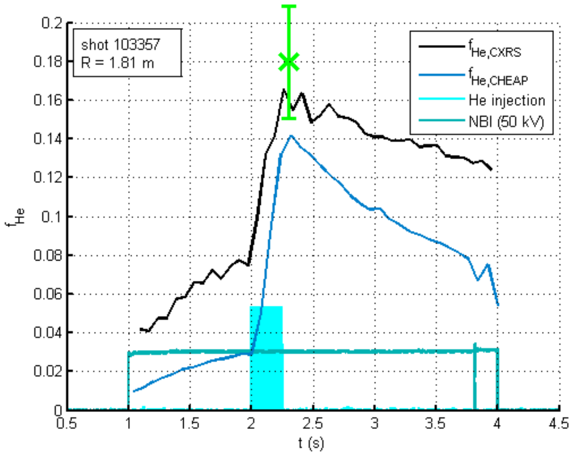

Figure 4.10 : *Direct measurement of the helium concentration, using active HeII-CX and BES intensities. After the helium puff at 2.0 s, the concentration is measured to be 16 %. For comparison the results from the CHEAP calculation and electron density are also shown.*

The final step towards the answer of the question posed at the start of this paragraph is now relatively small. First the measurement above of the helium concentration is expanded to all the lines-of-sight that are available. Then, multiplying that with the electron density profile as has been measured by the interferometer gives the measured helium density profile as a function of space and time, which is shown in Figure 4.11.

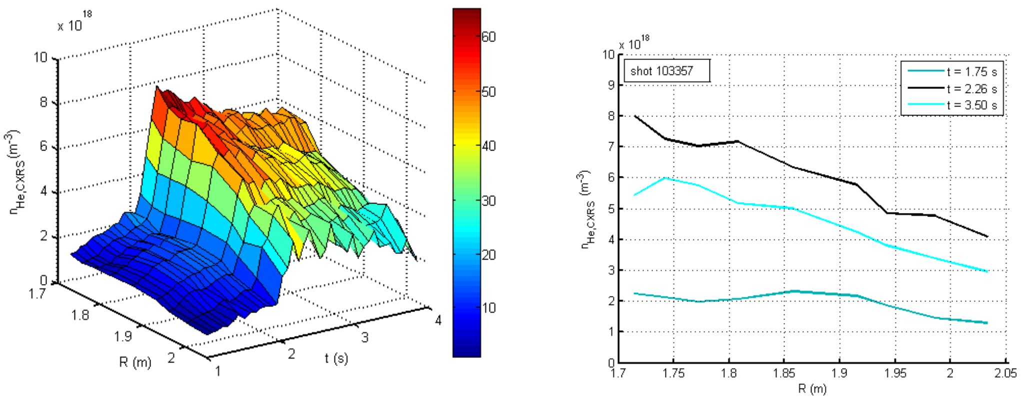

Figure 4.11 : *The measured helium density profile, derived from active HeII-CX and BES intensities, and calibrated on Bremsstrahlung emission.*

4.2.4 Comparison and discussion

In the first section of this paragraph the helium concentration is derived from electron density measurements during the injection of helium, and it is found to be (18 ± 3) %. The main advantage of this method is that the calculation is straightforward and that it requires just one diagnostic to do the measurement. Furthermore, the underlying physical assumptions are robust and will provide a solid value for the helium concentration. A weak point of the method is that it requires an estimate of the concentration prior to the injection, which can not be determined from the measurements itself. For the initial estimate of $f_{He}(t_1)$, measurements from the CXRS diagnostic had to be consulted, which slightly diminishes the strength of the method. The major shortcoming of this indirect measurement is however, that it requires a helium puff and therefore it is a snapshot measurement of f_{He}.

The main benefit of using the intensity of the active HeII-CX emission to determine the helium concentration is that it can continuously be measured and does not require an extra injection of helium nor an initial estimate. When using CHEAP for determining the neutral beam density from (2.25), there are however two major obstacles. The first drawback in the attenuation calculation follows from regarding the error propagation in (4.6). In [23] it is already shown that an error $\mathrm{d}(n_e\sigma^{eff})$ leads to the following error in the neutral particle density:

$$\frac{\mathrm{d}n_{beam}(r)}{n_{beam}(r)} = \ln\left(\frac{n_{beam}(r)}{n_{beam}(0)}\right)\cdot\frac{\mathrm{d}(n_e\sigma^{eff})}{n_e\sigma^{eff}}. \tag{4.10}$$

In case $\mathrm{d}(n_e\sigma^{eff})$ is about 10 %, this stands for an error margin of almost 25 % for a beam attenuation factor of 0.10 and nearly 50 % for a factor of 0.01. These attenuation factors are not uncommon near the plasma centre of a reactor such as ITER. For TEXTOR, the attenuation factor ζ in the centre is about 0.3 (cf. Figure 4.6), which results in an error margin of 20 %. The error in $\mathrm{d}(n_e\sigma^{eff})$ on its turn is dependent on e.g. n_e, T_e, and Z_{eff}. In case the latter is not measured by its diagnostic, a certain Z_{eff} profile has to be estimated an used as an input in CHEAP, which indirectly contributes to the error in the finally obtained helium density.

The second considerable difficulty in this method is that an absolute optical calibration is required for the measurement of the active HeII-CX intensity. The optical throughput for each line of sight should be measured and although the same fibres are used, this does not necessarily mean that the throughput is identical as well. As there are many lenses in the optical system, the depiction of fibres on the CCD-chip is always influenced by aberrations which can certainly differ from fibre to fibre. Since an absolute calibration also requires an opening of the vacuum vessel, it has not been possible to perform it for the whole system. Therefore equal calibration factors have been use as an input in CHEAP. It is probably due to this problem that the density profile of Figure 4.7 is not completely symmetrical around the plasma centre (at $R = 1.81\ m$).

The major difficulties concerning the use of CHEAP disappear when the BES intensities are measured simultaneously along the same lines-of-sight (i.e. through the same fibres) and using the same optics (i.e. suffering from the same aberrations). The same lines-of-sight guarantee that the neutral beam density measured by BES originates from the same observed volume as that from the HeII-CX intensities. This also ensures that the error margins on the helium density measurements are the same for each line-of-sight, whereas the ones calculated in CHEAP are integrated errors along the injection path of the neutral beam. Furthermore, using the same optics discards the need of an absolute calibration of the whole optical system. Compared to the electron density method, the main advantage of continuous measurement remains.

At first sight, there is a good agreement between the three methods on the helium concentrations after the injection, as shown in Figure 4.10. Within the error margins, they all overlap at that one moment. However, comparing the continuous methods of CHEAP and combined CXRS/BES, it seems that the CHEAP method systematically underestimates the helium concentration, especially prior to the puff and then again towards the end of the measurement. Due to the iterative nature of the CHEAP calculation, it is difficult to exactly identify the cause of the difference between the continuous measurements. The most probable cause is a small error in the initial estimates of e.g. the impurity concentrations in the plasma, which then grows in the iteration.

However, a major downside also appeared in the followed procedure for the combined CXRS/BES method. It has been assumed that the Bremsstrahlung emission, which is used for the relative calibration, shows similar behaviour at different wavelengths. Closer examination shows that this assumption is not valid, at least not for the performed experiment. In Figure 4.12 the Bremsstrahlung emissions are shown, determined from the BES (λ = 6561 Å) and HeII (λ = 4686 Å) spectra, and compared to the measurement of the Bremsstrahlung diagnostic.

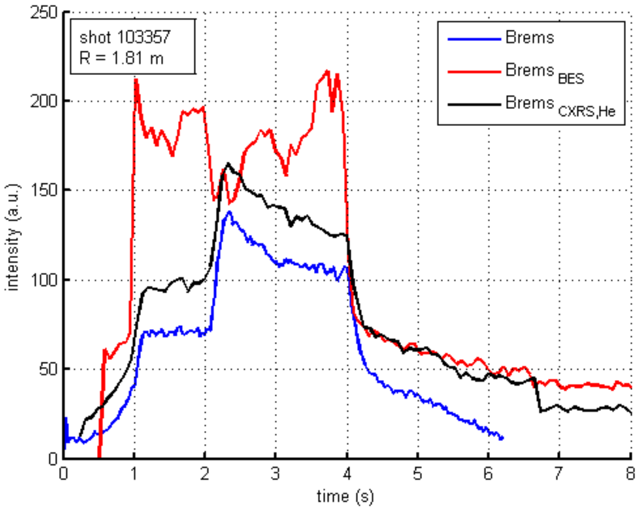

Figure 4.12 : *Bremsstrahlung intensities around the wavelengths of HeII-CX (black) and BES (red) compared to the signal of the Bremsstrahlung diagnostic (blue). It can clearly be seen that the behaviour of BES Bremsstrahlung is distinctively different from that of the dedicated diagnostic.*

The different behaviour of the Bremsstrahlung emission measured on the BES spectrum is most likely due to the fact that the lines-of-sight end on a part of the vessel that has started to emit black body radiation (possibly as a result of heating). These lines-of-sight are of course identical to the ones that measure the HeII emission, but since black body radiation is wavelength dependent, according to the Planck curve, this probably explains why it is not seen in the HeII Bremsstrahlung emission.

Overall, all three measurement methods have their results in the same ball park. So, this suggests that, with a careful procedure for the relative calibration, the combined CXRS/BES method for measuring f_{He} is equally valid to the one using CHEAP calculations.

Chapter 5

Helium transport

In this chapter, the measurements of helium density profiles from the previous chapter, and the transport theory introduced in Chapter 2 are combined. The first paragraph describes helium transport properties from the density profile evolution, which allows determination of both the diffusive as well as the convective transport coefficients. In the second paragraph, the effective confinement time τ^*_{He} is derived from the density decay, and the effect of different perturbation fields induced by the DED on τ^*_{He} is investigated.

5.1 Determining transport coefficients

The density measurements from paragraph 4.2, in the transient phase of helium injection, are interpreted in the first section of this paragraph, where they are compared to a simple numerical simulation. In the second section, the method described in section 2.1.2 is used to derive the ratio of the diffusion and convection coefficients in the steady state phase, after the injection.

5.1.1 Diffusion and convection in the transient phase

The density profiles shown in paragraph 4.2 (Figure 4.11) are measured as a function of the major radius R (m). However, the diffusion equation of (2.11), from which the transport coefficients D and V are derived, is to be interpreted in terms of flux surface coordinates (on which temperature, density and pressure are constant). The transformation of major radius to the flux surface coordinate ρ is done with the use of the Shafranov-shift, which has been derived from measurements of β_p and the plasma position relative to the major radius R_0 of TEXTOR. The range of major radii from 1.77 m to 1.98 m, determined from BES as described in section 2.2.3, is converted to $\rho = 0.0 - 0.4$ in this way. The uncertainty margins, originating from crossing several flux surfaces as shown in Figure 3.6, are also accordingly converted.

The left graph of Figure 5.1 shows the density profile as a function of flux surface coordinate and time. The density as a function of ρ is shown in the left graph of Figure 5.2 for a few instants in the transient phase (cf. Figure 2.4). As can be seen in this figure, accurate determination of the density gradient $\nabla n_{He}(r)$ is problematical due to the large uncertainties, especially in position but also in the density measurement. For the latter, only the statistical errors are shown; they originate from the Gaussian fit to the observed HeII-CX intensity, and incorporate the statistical uncertainty that arises in collecting the emitted photons. Systematic errors that could also occur in the density measurement, e.g. those caused by errors in the used CX or beam emission cross-sections or the calibration, are not shown since they will not change the profile shape (only raise or lower it as a whole). Consequently, determining D and V separately from this measurement according to the method of 2.1.2 will be troublesome, taking into account that the uncertainties also apply to the flux density (2.12).

However, regardless of the uncertainties, it is still possible to give an interpretation of the measurement in terms of D and V, by comparing it to numerical modelling of the transport equation (2.10). An applicable model is found in [43], where (impurity) densities are calculated for discrete time steps on a radial mesh grid from the transport equation:

$$\frac{\partial n}{\partial t} = \frac{1}{r}\frac{\partial}{\partial r}\left(r\left(D\cdot\frac{\partial n}{\partial r} - Vn \right)\right) - \frac{n}{\tau_{\parallel}} + R(n) + Q\,. \tag{5.1}$$

This expression incorporates a term for the parallel loss with a characteristic decay time $\tau_{\parallel}$ in the Scrape-Of-Layer (SOL), and a term $R(n)$ for the ionization and recombination processes. However, parallel losses do not appear within the boundaries of the modelled volume (i.e. $\tau_{\parallel}$ is chosen to be large, 10^3 *s*), and all helium particles are assumed to be ionized within there (so $R(n)$ does not play a role). The expression remaining of (5.1) for the transport coefficients D and V, and the external source term Q is then identical to (2.10) and (2.11).

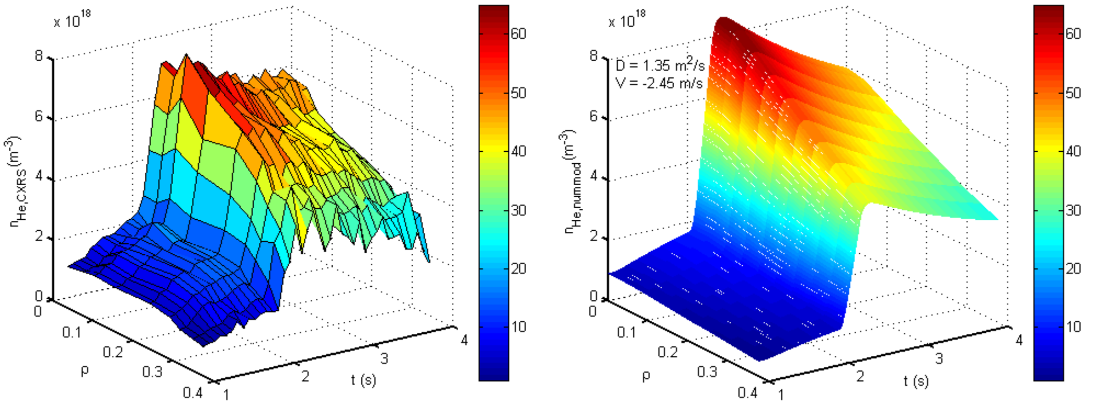

Figure 5.1 : *Helium density profiles as a function of time and the normalized radius. The left graph shows the density from the combined He-CX and BES measurement of Figure 4.11 converted to ρ. In the right graph, the result of the numerically iterated transport equation* (2.11) *is shown.*

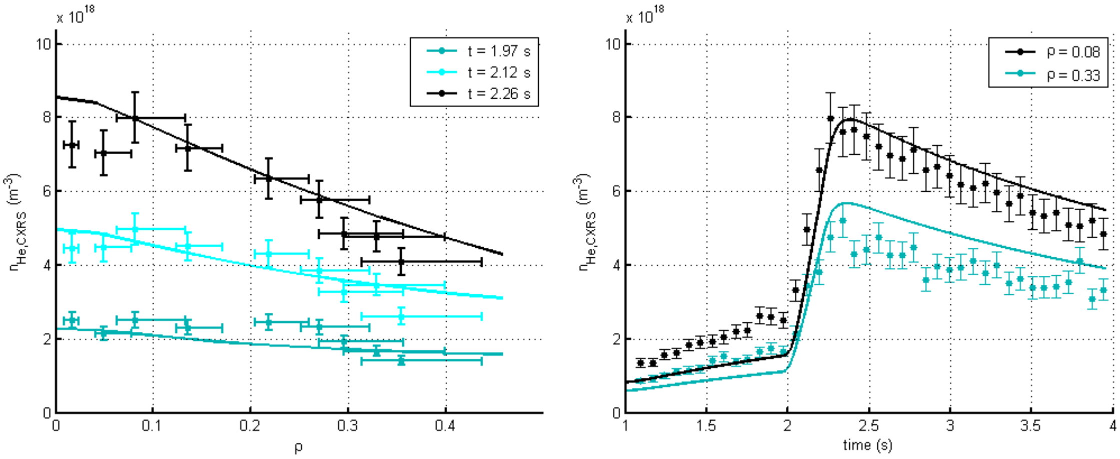

Figure 5.2 : *In the left graph, helium density profiles are shown as a function of ρ for three moments during the helium injection phase. The right graph shows density time traces for the measurements at ρ = 0.08 and ρ = 0.33. In both graphs, the measured data is shown with accompanying (statistical) error bars, and the full drawn lines originate from the numerical modelling of the transport equation.*

Discretisation of (5.1) can be done using a time-centred Crank-Nicolson scheme, where the change of density at a radial grid point r during a time-step Δt is calculated by taking spatial derivatives of the density at $t = t + \frac{1}{2}\Delta t$. Using step number l and $n^{l+1/2} = \frac{1}{2}(n^l + n^{l+1})$, it follows for the time-discretisation of (5.1) that

$$\frac{n^{l+1} - n^l}{\Delta t} = D\frac{\partial^2 n^{l+1/2}}{\partial r^2} + \left(\frac{D}{r} + \frac{dD}{dr} - V\right)\frac{\partial n^{l+1/2}}{\partial r} - \left(\frac{V}{r} + \frac{dV}{dr}\right)n^{l+1/2} + Q. \tag{5.2}$$

When the spatial derivatives are then discretised as well, this approach gives an unconditionally stable numerical method and yields a solvable (Thomas algorithm) tri-diagonal matrix equation on all mesh points [43], [44].

The performed numerical calculations, based on the above given discretisation method of the transport equation (5.2), are completed with the following boundary conditions and approximations:

- at the inner boundary (the plasma centre $r = 0$), the density gradient and the velocity coefficient V are zero;
- at the outer boundary, the density is set to decay with $d_r(n) = -n/\lambda$, using a fictitious extra grid point and a typical decay length λ (a condition from plasma-edge and SOL physics, strongly determined by e.g. pumping efficiencies);
- the diffusion and convection coefficients D and V are assumed to be constant in between the two boundaries: $D = 1.35\ m^2/s$ and $V = -2.45\ m/s$;
- the mesh grid is defined by time-steps of 1 *ms*, and 25 equidistant normalized radial sections;
- a constant source of helium particles is present at the edge during the use of the NBI (assumed to be due to increased streaming from the wall);
- the helium gas puff is modelled as a temporary source Q from the outermost edge to three grid points inward.

The result of this numerical calculation is shown, as a function of normalized radius and time, in the right graph of Figure 5.1 (for comparison to the measurements on the left). The full drawn lines in Figure 5.2 are excerpts from the same calculation, at moments and radii comparable to those of the measurements. Comparing the measurements and the numerical model in Figure 5.1, it can be seen that they resemble each other rather well for the chosen values of D and V; deviations occur at the plasma centre and near $\rho = 0.4$, where the model slightly overestimates the helium densities. The same resemblance is found when the measurements with their error margins are compared to the model in the graphs of Figure 5.2. So, taking into account the rather crude assumptions made for the model, and the large margins on the measurements, it seems that the values ($D = 1.35\ m^2/s$ and $V = -2.45\ m/s$) for the transport coefficients are in the ball-park of what can be expected [45], [46]. Note that these values are not resulting from an optimized fit. With a deviation of more than 2 % for D and for V, however, the results from the model will not resemble the measured density profiles anymore.

5.1.2 Transport coefficients in steady state

A second method to derive the convective and diffusive transport coefficients from the measured helium density profiles follows from (2.13). It is based on the fact that the density flux is zero in the steady state phase (i.e. after the helium injection), from which it follows that the ratio V/D is equal to the relative density gradient as a function of the radial position.

In the steady state phase, the density profiles maintain their radial shape and decrease as a whole. This provides an opportunity to decrease the density error margin by averaging over several subsequent measurements, and so obtain a more accurate profile.

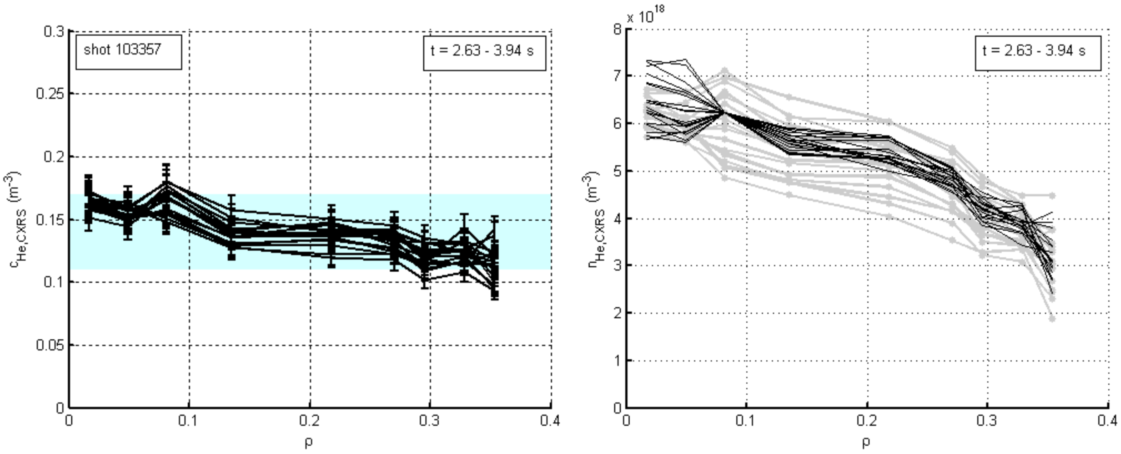

Figure 5.3 : *Helium density profiles in the steady state phase: the left graph shows that the helium concentration profiles remain flat within the error bars. Therefore, as is shown in the right graph, all density profiles of the steady state phase (in grey) can be normalized relative to one point at* $\rho = 0.08$ *(in black).*

The constant profile shape is revealed in the left graph of Figure 5.3, where the helium concentration profiles are shown to be flat, within the error margins, throughout the observed range of flux surfaces. The right graph in Figure 5.3 shows (in grey) all the measured density profiles in the steady state phase. With their constant profile shapes, they can then be normalized to one point from an arbitrary profile, as is shown by the black curves in the same graph. Combining these normalized profiles results in an average helium density profile for the steady state phase with decreased error margins, as is shown below in Figure 5.4. The drift parameter V/D, shown in blue in the same graph, can then be determined with (2.13) from the (black) curve that matches the averaged helium profile. For the observed radii, V/D varies between 0 m^{-1} (in the centre) and -8 m^{-1} near $\rho = 0.4$.

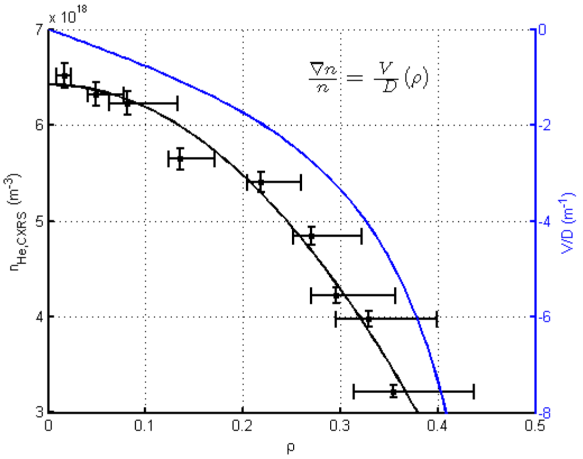

Figure 5.4 : *Average helium density profile in the steady state phase, resulting from the normalized density profiles of Figure 5.3. The error bars on density are diminished by averaging, but the uncertainties in* ρ *remain. To guide the eye, a full (black) line is drawn through the measurements, from which the drift parameter V/D (blue) is derived using (2.13).*

5.1.3 *Intermediate comparison and discussion*

In the previous paragraphs, two different methods have been described to retrieve information, in the form of transport coefficients, on the behaviour of helium in the plasma. The advantage of the first method is that it provides separate values for V (-2.45 m/s) and D (1.35 m^2/s). The second method, however, has shown that their ratio is a function of the flux surface coordinate ρ, and varies between 0 m^{-1} (in the centre) and -8 m^{-1} near $\rho = 0.4$. The ratio of V and D from section 5.1.1 ($\approx$ -1.8), where both are assumed constant in the model, is well within this range. Nevertheless, the result from section 5.1.2 suggests that the model can be improved using transport coefficients that are flux surface dependent.

When (2.10) and (2.11) are combined, without the helium source S_{He}, it is possible to relate the D and V to the helium particle confinement time τ_{He}. Please note that in order to link the global quantity τ_{He} to the principally local quantities D and V, the latter have to be assumed constant over whole plasma region again. The following simple one-dimensional approximation for the helium density distribution can then be used

$$n_{He^{2+}}(\rho,t) = n^0_{He^{2+}} \cdot \exp\left(-\frac{t}{\tau_{He}}\right)\exp\left(-\frac{\rho}{l}\right), \tag{5.3}$$

where l is the diffusion length, and n^0 is an initial density distribution. The relation between D, V, and τ_{He} now follows from applying (2.10) and (2.11) to (5.3), which results in:

$$\tau_{He} = \frac{l^2}{D - V \cdot l}\,. \tag{5.4}$$

With the constant values for D and V found in 5.1.1, and assuming the diffusion length l to be equal to the plasma minor radius (i.e. 0.47 m), τ_{He} is estimated to be 88 ± 2 ms. However, this τ_{He} does not include the effect of particles flowing back into the plasma core via desorption and/or reflection from the wall. When trying to match the model from section 5.1.1 to the measurements, it was found though that these effects can be of large influence (see the list of boundary conditions). According to (2.14), the effects can be accounted for when an effective recycling coefficient R_{eff} is used, which results in an effective particle confinement time τ^*_{He}. The next paragraph describes how τ^*_{He} can be measured and how the DED (section 3.1.3) is used to try and change R_{eff} in order to influence the effective particle confinement time.

5.2 The effect of the DED on helium confinement

As discussed in the last part of section 2.1.2, the helium density decay phase after an injection is not only suited for deriving the drift parameter V/D (as performed in the previous paragraph), but it also yields the possibility of measuring τ^*_{He} according to (2.15). In this paragraph, τ^*_{He} will be determined in this way for three different DED currents, investigating the influence of the perturbation field on the helium confinement time ratio ρ (1.5).

Using the results obtained from the measurements of Chapter 4 (as shown in Figure 4.11, Figure 5.2, and the graphs of Figure 5.5 and Figure 5.6 below), it is possible to derive τ^*_{He} using an exponential fit that describes the density decay as:

$$n_{He^{2+}}(t) = n^{backg.}_{He^{2+}} + n^{inj.}_{He^{2+}} \cdot \exp\left(-\frac{t}{\tau^*_{He}}\right). \tag{5.5}$$

Here, $n^{backg.}$ is the background density (taken to be the average of the last three measurements before the injection), and $n^{inj.}$ is the magnitude of the gas puff relative to the background density.

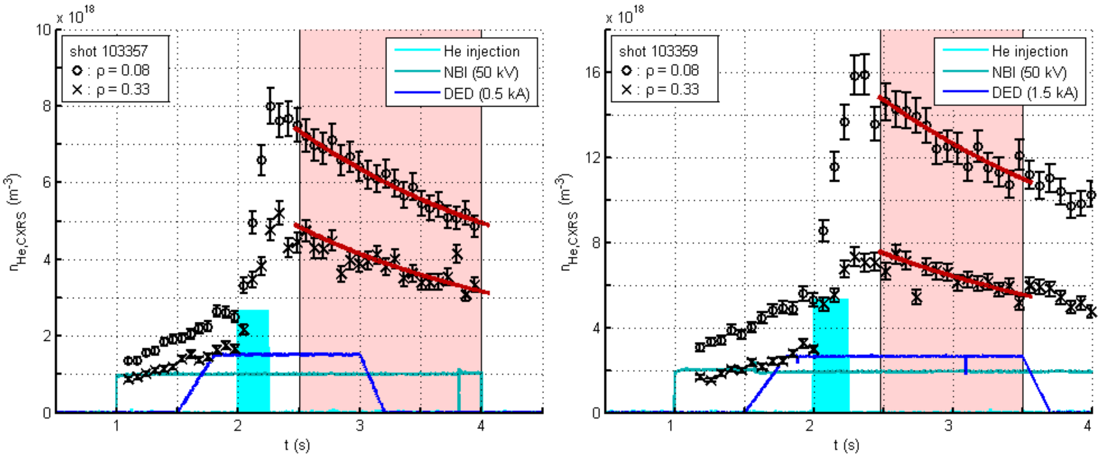

Figure 5.5 : *In these graphs, the helium density decay after a gas puff is shown for two discharges with different DED AC*$^{-}$ *currents (0.5 kA and 1.5 kA). The decay times* τ^*_{He} *have been determined at* $\rho = 0.08$ *and* $\rho = 0.33$ *for the indicated phases.*

The energy confinement time τ_{E} can easily be determined from measurements of the diamagnetic energy E_{dia}, the radiation loss P_{rad}, and the input powers P_Ω and P_{NBI} (Ohmic and neutral beam heating), using:

$$\tau_E \equiv \frac{W}{\mathrm{d}W/\mathrm{d}t} = \frac{\int \frac{3}{2}\left(n_e kT_e + n_i kT_i\right)\mathrm{d}V}{P_{transport}} = \frac{E_{dia}}{P_\Omega + P_{NBI} - P_{rad}}, \tag{5.6}$$

where W is the total plasma energy. Although another definition of the energy confinement time ($\tau_{\mathrm{E}} \equiv E_{dia}/P_{input}$) is more commonly used in literature [48], the closed curves of the confinement time ratio ρ in section 2.1.1 have been derived using this definition.

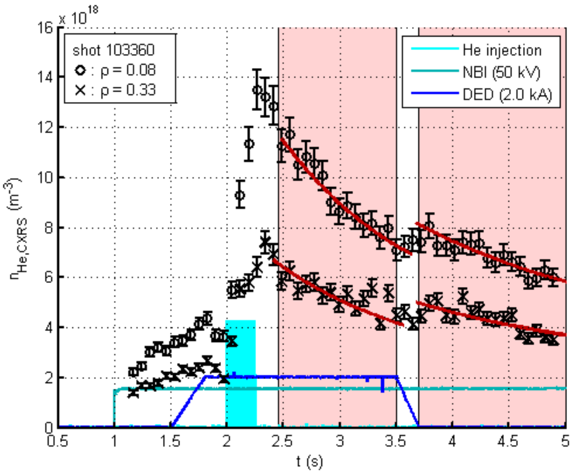

Figure 5.6 : *Helium density decay for a discharge with and without a DED (AC*$^{-}$ *current of 2.0 kA) phase. The observation time for this measurement was sufficient to distinguish between phases with and without DED. From ECE-measurements it was however found that a 2/1 tearing mode was triggered by the DED current.*

In Figure 5.7 the measurements of τ_E, using the definition of (5.6), are shown for the same discharges as in Figure 5.5 and Figure 5.6. As indicated, a constant τ_E has been assumed for the phases for which τ^*_{He} has also been determined.

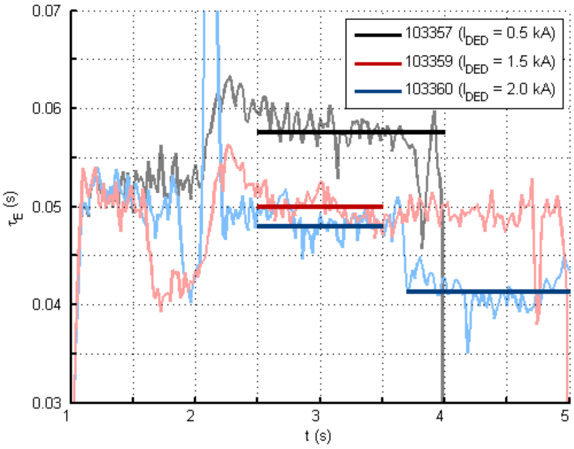

Figure 5.7 : *Measurements of energy confinement times for the discharges shown in Figure 5.5 and Figure 5.6, calculated according to (5.6). The straight lines (in black, red, and blue) indicate the average values of* τ_E *for the different phases for which* τ^*_{He} *has been determined.*

Investigation of the influence of the magnetic perturbation field of the DED, can now be performed by varying the DED AC^{-} currents and accordingly measuring the confinement time ratios. In Figure 5.5 and Figure 5.6, the helium decay is shown for measurements at two different normalized radii (ρ = 0.08 and ρ = 0.33). As can be seen in Table 5.1, which gives an overview of the results, the decay times at both radii are the same within the error margins for all measurements. This is evidently due to the self similar way in which the density decreases in the steady-state phase, as was already described in the previous paragraph. Therefore these decay times can be averaged when determining the confinement time ratio ρ. For the discharge where a current of 2.0 kA was applied (Figure 5.6), the observation time was long enough to distinguish between a phase with DED perturbation and phase without. Whereas for the discharge shown in the left graph of Figure 5.5, τ^*_{He} has been determined for one phase with and without DED.

Increasing the DED current from 0.0 - 1.5 kA, thereby trying to alter R_{eff} in (2.14), is not directly reflected in the measurements of τ^*_{He} as can be seen in the first row of Table 5.1. Averaging for ρ = 0.08 and ρ = 0.33, and using τ_{He} (88 ± 2 ms) as calculated in section 5.1.3, the effective reflection coefficient is found to be 96 ± 1 % for these three DED currents. The fact that the plasma position relative to the ALT-II pump limiter was not optimized for the performed experiments is the most likely reason for not observing large changes in τ^*_{He}.

Table 5.1 : Helium decay rates, energy confinement times and their ratios for varying DED currents.

		I_{DED} = 0.0 kA (103360 – II)	I_{DED} = 0.5 kA[†] (103357)	I_{DED} = 1.5 kA (103359)	I_{DED} = 2.0 kA (103360 – I)
τ^*_{He} (s)	ρ = 0.08	1.84 ± 0.55	2.14 ± 0.21	2.12 ± 0.44	1.24 ± 0.63
	ρ = 0.33	2.15 ± 0.93	1.97 ± 0.65	2.01 ± 0.97	1.28 ± 0.87
τ_E (ms)		41.3 ± 2.6	57.7 ± 2.3	49.9 ± 1.6	48.0 ± 2.0
ρ		48 ± 13	36 ± 6	41 ± 11	26 ± 11

[†] As can be seen in the left graph of Figure 5.5, τ^*_{He} has been determined for a single phase with and without DED.

However, when an AC$^-$ current of 2.0 *kA* is applied, the helium decay time shortens significantly from about 2.04 *s* to 1.26 *s*. This effect, though, is due to the occurrence of a large 2/1 tearing mode, a magnetic perturbance known to have a large influence on particle transport in the plasma. The presence of this island is demonstrated by the disappearance of the electron temperature sawtooth oscillation in the plasma centre, as measured by ECE. So in this case, an effect on τ_{He} (2.14) is observed rather than on R_{eff}. A noteworthy observation can be done, when the discharges with DED currents of 1.5 *kA* (without a magnetic island) and 2.0 *kA* (with an island) are compared. The energy confinement times τ_E, namely, are the same in both discharges, whereas it is normally observed that magnetic islands not only decrease the particle but also the energy confinement time. This behaviour can clearly be seen for the 2.0 *kA* I_{DED} discharge in Figure 5.7, where τ_E decreases suddenly at the same time an island is formed (≈ 1.8 *s*). A similar decrease in τ_E is observed in the 1.5 *kA* I_{DED} discharge at about 1.60 *s*, but the sawtooth oscillation does not disappear in this case. The cause of the decrease in τ_E almost certainly is a short disturbance in the vertical plasma position at 1.59 *s*. Via the TEXTOR control system, this event has been followed by an injection of hydrogen (from about 1.66 *s* to 2.03 *s*). However, τ_E was not recovered to its previous value by the time the helium puff was started (2.00 *s*), which might explain the low energy confinement time for this discharge.

Overall, the achieved values for the helium confinement time ratio, both with and without the presence of a 2/1 tearing mode, are much larger than the goal of $\rho \leq 9$ (1.5). They are also larger than what has previously been reached on TEXTOR [11], [13], but still within the range of values that can be expected for L-mode discharges on limiter tokamaks [46]. Again, a better performance in terms of ρ can probably be attained when the plasma position is optimized towards the pump limiter.

Chapter 6

Conclusions

All the results from previous chapters are combined in the first paragraph of this chapter to answer the three questions posed at the end of Chapter 1. To end with, in the second paragraph, a short outlook will be given towards possible improvements of the diagnostic system and relevant plasma physics research areas.

6.1 On the behaviour of helium

As was brought up in the introduction of Chapter 1, monitoring the conduct of (thermal) helium will be an important aspect in the control of fusion reactors. The critical parameter in its behaviour is the confinement time ratio ρ, which relates the helium particle throughput to the plasma thermal insulation. The first is associated with the effective global helium particle confinement time τ^*_{He}, and the latter with the energy confinement time τ_E. Since τ^*_{He} is derived from the helium density, the work described in this thesis has mainly considered the three subjects of:

- how to measure helium densities;
- how to derive transport coefficients from these measurements;
- and how to try and manipulate the helium behaviour;

as was posed by the three questions at the end of Chapter 1.

The answer to the first question, on the possibilities for measuring helium densities, is extensively discussed in Chapter 4, where three methods for determining the helium concentration in a plasma are compared. The first method uses a gas puff for deriving the helium concentration from electron density measurements. The second and third method rely on measurements of the emission of helium ions, excited by a charge exchange reaction with hydrogen particles from the neutral beam.

Major advantages of the first method are that the calculation, based on solid physical assumptions, is straightforward and that the measurement is done by a fast, reliable diagnostic that is commonly available on all tokamaks. The important limitation for this method is that it requires an extra particle injection, generally undesirable, and therefore is a one instant measurement of the helium concentration only.

Both of the methods based on HeII CX emission, however, are able to provide continuous measurements of the helium density. When using the analysis package of CHEAP for determining a helium density profile, as is the standard procedure, it suffices to use only one spectrometer to measure the HeII CX intensity. This also implies, though, that the optical throughput has to be calibrated, preferably on a regular basis and over the whole optical system, which is usually not trouble-free. Furthermore, the neutral beam density that is calculated by CHEAP suffers from increasing error propagation towards the centre of the plasma. The code also requires the input of electron density, temperature, and effective charge profiles for its iterative calculations, and is strongly dependent on impurity concentrations and the values for beam emission reaction rates.

Most of these difficulties are overcome by combining the HeII CX intensity with that of beam emission, measured simultaneously on a second spectrometer, along the same lines-of-sight, and through the same optical system. In this way, the calculation of the neutral beam density via CHEAP becomes redundant, as well as the need for an absolute calibration of the optical system. What remains is the dependency of the CXRS and BES reaction rates on impurity densities, but this equally concerns both methods depending on HeII CX emission.

The good agreement found in comparing the helium densities as measured by the three methods, gives confidence in routinely taking the combined CXRS/BES method in use. The iterative procedure where CHEAP calculates the neutral beam density, using Z_{eff} profiles and BES reaction rates, has worked well for the performed experiments but should generally be carried out with awareness. The rather stable way the intensity of the active HeII CX emission is derived from the complex helium spectrum, using KS4FIT, adds greatly to this confidence.

The answer to the question whether helium transport coefficients can be derived from the measurements (using the combined CXRS/BES method) is twofold. According to the transport theory described in Chapter 2, the transport coefficients of diffusion and convection can separately be determined from density profile evolution after a gas puff.

However, due to the geometry of the observation system, the density profile measurements suffer from such large uncertainties in the flux surface coordinates that it is unfeasible to perform this derivation. Furthermore, separate determination of the transport coefficients is only possible in the transient phase of the gas puff, and the time-resolution of the observation system is only capable of capturing three to five instants during this phase.

During the steady state phase, which lasts considerably longer, enough density profiles can be captured to produce an average helium density profile. From this profile, however, only the ratio of the transport coefficients can be determined, and the uncertainties in flux surface coordinates remain present. This method does reveal though, that the transport coefficients can not be assumed constant over the whole plasma.

The helium density decay in the steady state phase also yields the possibility of measuring the effective helium confinement time τ^*_{He} with an accuracy of about 30 %.

When the measurements of τ^*_{He} are combined with the energy confinement time τ_E, the confinement time ratio ρ can easily be determined. For all the performed discharges, the obtained values were three to five times larger than the goal of $\rho \leq 9$ required for maintaining a burning plasma. These values are in the range of what is expected for L-mode discharges on limiter machines, where the exhaust is restricted by the pumping efficiency rather than the transport properties of the plasma. Since transport properties of the plasma and pumping efficiency are less directly linked in case of a divertor configuration, it is expected that the requirement of $\rho \leq 9$ will be reached for ITER [46].

However, in order to increase the operational space for an effective fusion process, it is in general desirable to achieve much lower values then just $\rho = 9$. Therefore, taking up the last question, an attempt to influence the helium exhaust was made by using the properties of the DED, a special feature on the TEXTOR tokamak. By increasing the current running through these perturbation coils, it was supposed that the induced laminar zones would increase and lead to particles remaining longer in the plasma edge. This should have a direct influence on the pumping efficiency and the effective recycling coefficient R_{eff}, and consequently on τ^*_{He} and ρ as well. Such an effect, however, has not been observed in the performed experiments, though it was found that τ^*_{He} decreases about 35 % in the presence of a large 2/1 magnetic island that was triggered by a high DED current (2.0 *kA*).

The most plausible explanation for the fact that no difference in τ^*_{He} has been observed for lower DED currents (0.0 - 1.5 *kA*), is that the last closed flux surface (LCFS) of the plasma was not in interaction with the pumped limiter; i.e. the plasma position relative to the ALT-II tiles was not optimized. The decrease of τ^*_{He} in the presence of a magnetic island has to be attributed to a change in the particle confinement time τ_{He} rather than in the recycling coefficient R_{eff} in τ^*_{He}.

6.2 Outlook

Based on the conclusions from the previous paragraph, and the experience gained from the work described in the preceding chapters, some points for improving the measurement method and a few areas of relevant plasma physics are pointed out in this last paragraph.

Although the helium density has been measured with confidence for the work of this thesis, room for improvement of the diagnostic system can still be found in the following suggestions:

- even though the relative calibration in the combined CXRS/BES method is much less demanding than an absolute calibration, it should still be made sure that the background intensity level is attributed to Bremsstrahlung emission only (and no black-body radiation);
- confidence in the results of the CHEAP calculations of the neutral beam density/attenuation will be increased when the Z_{eff} diagnostic at TEXTOR is taken into more regular use, so its measurements can be included in the calculations;
- although the used CCD camera is not capable of doing so, it would be worthwhile to test a (frame transfer) camera with a time resolution of 5-10 *ms*, which provides more profile measurements in the transient phase of a gas puff; as that also complies with ITER requirements [51], it would add to the TEXTOR CXRS setup as an ITER test facility;
- taking the ITER-pilot top view system in use, with viewing lines up to the plasma centre, will greatly enhance the measurements of the spatial density distribution: better place resolution (more lines-of-sight), and much smaller uncertainties in the flux surface coordinates (geometry effect); with a change over from prism to mirror, this system has recently been taken into regular operation and now benefits from these improvements.

As far as the field of (plasma) physics is concerned, it must first be stated that for the helium exhaust experiments described in this work, the position of the LCFS relative to the pumped limiter has proven to be of crucial importance. In case future experiments are to be performed where TEXTORs DED is used in order to change edge properties and hence helium exhaust, the plasma position should be taken into consideration very precisely. However, based on the work of this thesis, the following prominent topics could also be addressed:

- closely related to the experiments described in this thesis, are those carried out on the so-called particle pump out effect: in these recently developed plasma scenarios it is investigated whether particle transport near the plasma edge is governed by edge islands, that are induced already at low DED currents [33], [50];
- in case a faster CCD camera is to be used, it might be worthwhile to perform modulated gas puff experiments (which provide another method to derive diffusion and convection terms separately) as proposed in [51];
- one other candidate for controlling the helium conduct is sawtooth oscillation, which is known to produce large particle outbursts from the centre [52]; it is one of the proposed methods to remove accumulated helium ash from the centre of a burning plasma, and it could well be monitored using the CXRS method of measuring helium densities;
- a second option for investigation of the helium behaviour in the plasma, is by coupling ICRH waves to (thermalised) helium particles in order to expel them from the plasma centre [53], [54];

To conclude this work with, the confidence with which the thermal helium spectrum can now be analysed opens the possibility for measuring fast helium. As the fusion reaction in ITER will create α-particles, investigating its behaviour and possible (Alfvén) instabilities will be of great importance. For research at TEXTOR fast helium could be created by using e.g. ICRH minority heating, or helium neutral beams. If monitoring fast helium can successfully be performed, this might be added to tasks of the CXRS diagnostic on ITER. Further research is then still required in order to assess the optimal qualifications of CXRS and its compatibility with such techniques as collective Thomson scattering (CTS) [55].

Bibliography

[1] A. Einstein. *"Ist die Trägheit eines Körpers von seinem Energieinhalt abhängig?"* Ann. Phys., Folge 4, Band 18, Heft 13, p.639 (1905).

[2] H.-S. Bosch and G.M. Hale. *"Improved formulas for fusion cross-sections and thermal reactivities."* Nucl. Fusion, Vol.32, No.4, p.611 (1992).

[3] J.D. Lawson. *"Some criteria for a power producing thermonuclear reactor."* Proc. Phys. Soc. B, Vol.70, No.1, p.6 (1957).

[4] D. Reiter, G.H. Wolf, and H. Kever. *"Burn condition, helium particle confinement and exhaust efficiency."* Nucl. Fusion, Vol.30, No.10, p.2141 (1990).

[5] J. Goedbloed. *"Toroidal theory of MHD instabilities."* Fusion Sci. Technol., Vol.45, No.2T, p.95 (2004).

[6] J. Wesson. *"Tokamaks."* Oxford University Press, Great Clarendon Street, Oxford OX2 6DP, 2nd ed. (1997).

[7] E. Rebhan et al. *"Effect on helium concentration curves with energy confinement time including radiation losses."* Nucl. Fusion, Vol.36, No.2, p.264 (1996).

[8] J. Hogan, *"Helium transport and exhaust experiments in tokamaks."* J. Nucl. Mat., Vol.241-243, p. 68 (1997).

[9] D.S. Gray et al. *"Plasma exhaust requirement for sustained ignition: relaxation due to profile considerations."* Nucl. Fusion, Vol.37, No.10, p.1437 (1997).

[10] D. Reiter et al. *"Helium removal from tokamaks."* Plasma Phys. Contr. Fusion, Vol.33, No.13, p.1579 (1991).

[11] D.L. Hillis et al. *"Helium exhaust and transport studies with the ALT-II pump limiter in the TEXTOR tokamak."* Phys. Rev. Lett., Vol.65, No.19, p.2382 (1990).

[12] M.G. von Hellermann et al. *"Overview of recent impurity transport experiments on TEXTOR."* 31st EPS Conf. on Plasma Physics (London), ECA, Vol. 28G, P.-1.118 (2004).

[13] K.H. Finken. *"Particle, in particular helium removal experiments optimized by the dynamic ergodic divertor."* Fusion Eng. Des. Vol.37, Iss.3, p.445 (1997).

[14] R.C. Isler. *"An overview of charge-exchange spectroscopy as a plasma diagnostic."* Plasma Phys. Contr. Fusion, Vol.36, No.2, p.171 (1994).

[15] M.F.M. De Bock. *"Understanding and controlling plasma rotation in tokamaks."* Ph.D. thesis, Technische Universiteit Eindhoven (2007).

[16] M.G. von Hellermann et al. *"Analytical approximation of cross-section effects on charge exchange spectra observed in hot fusion plasmas."* Plasma Phys. Control. Fusion, Vol.37, No.2, p.71 (1995).

[17] NIST Atomic Spectra Database, http://physics.nist.gov/PhysRefData/ASD/.

[18] M.G. von Hellermann et al. *"Complex spectra in fusion plasmas."* Physica Scripta, Vol.T120, p.19 (2005).

[19] M. Tunklev et al. *"Modelling of passive charge exchange emission and neutral background density deduction in JET."* Plasma Phys. Control. Fusion, Vol.41, No.8, p.985 (1999).

[20] U. Gerstel et al. *"Quantitative simulation of non-thermal charge-exchange spectra during helium neutral beam injection."* Plasma Phys. Control. Fusion, Vol.39, No.5, p.737 (1997).

[21] M.G. von Hellermann et al. *"Observation of alpha particle slowing-down spectra in JET helium beam fuelling and heating experiments."* Plasma Phys. Control. Fusion, Vol.35, No.7, p.799 (1993).

[22] A. Boileau et al. *"Observations of motional Stark features in the Balmer spectrum of deuterium in the JET plasma."* J. Phys. B: At. Mol. Opt. Phys., Vol.22, L145 (1989).

[23] W. Mandl et al. *"Beam emission spectroscopy as a comprehensive plasma diagnostic tool."* Plasma Phys. Contr. Fusion, Vol.35, No.10, p.1373 (1993).

[24] F.M. Levinton et al. *"Magnetic field pitch-angle measurements in the PBX-M tokamak using the Motional Stark Effect."* Phys. Rev. Lett., Vol.63, No.19, p.2060 (1989).

[25] O. Neubauer et al. *"Design features of the tokamak TEXTOR."* Fusion Sci. Technol., Vol.47, No.2, p.76 (2005).

[26] K.H. Finken et al. *"The toroidal pump limiter ALT-II in TEXTOR."* Fusion Sci. Technol., Vol.47, No.2, p.126 (2005).

[27] R. Koch et al. *"Ion Cyclotron Resonance Heating on TEXTOR."* Fusion Sci. Technol., Vol.47, No.2, p.97 (2005).

[28] E. Westerhof et al. *"Electron Cyclotron Resonance Heating on TEXTOR."* Fusion Sci. Technol., Vol.47, No.2, p.108 (2005).

[29] I.G.J. Classen. *"Imaging and control of magnetic islands in tokamaks."* Ph.D. thesis, Technische Universiteit Eindhoven (2007).

[30] R. Uhlemann and J. Ongena. *"Variation of injected neutral beam power at constant particle energy by changing the beam target aperture of the TEXTOR neutral beam injectors."* Fusion Sci. Technol., Vol. 35, No.1, p.42 (1999).

[31] A.J.H. Donné et al. *"Overview of core diagnostics for TEXTOR."* Fusion Sci. Technol., Vol. 47, No.2, p.220 (2005).

[32] K.H. Finken et al. *"Special Issue: Dynamic Ergodic Divertor."* Fusion Eng. Des., Vol.37, Iss.3, p.335 (1997).

[33] O. Schmitz. *"Overview on first results on edge transport in m/n = 6/2 base mode configuration."* TEXTOR TG Tokamak physics meeting (2007).

[34] M.W. Jakubowski et al. *"Modelling of the magnetic field structures and first measurements of heat fluxes for TEXTOR-DED operation."* Nucl. Fusion, Vol.44, No.6, p.S1 (2004).

[35] M.G. von Hellermann et al. *"Status of the DNB based ITER CXRS and BES diagnostic."* Rev. Sci. Instr., Vol.77, No.10, Art. 10F516 (2006).

[36] F. Glass. *"Private communications."* (2007).

[37] C. van Essen. *"Master thesis on Beam Emission Spectroscopy."* Universiteit Leiden (2007).

[38] M. von Hellermann et al. *"Pilot experiments for the Internation Thermonuclear Experimental Reactor active beam spectroscopy diagnostic."* Rev. Sci. Instr., Vol.75, No.10, p.3458 (2004).

[39] H. Morsi et al. *"A visible and UV charge exchange spectroscopy system for the tritium phase of JET."* Plasma Phys. Control. Fusion, Vol.37, No.12, p.1407 (1995).

[40] M.G. von Hellermann. *"Private communications."* (1995, 1996).

[41] H. Anderson et al. *"Neutral beam stopping and emission in fusion plasmas I: deuterium beams."* Plasma Phys. Control. Fusion, Vol.42, No.7, p.781 (2000).

[42] Atomic Data and Analysis Structure, http://adas.phys.strath.ac.uk/.

[43] R. Dux. *"Impurity transport in tokamak plasmas."* Habilitationsschrift, Max-Planck-Institut für Plasmaphysik, Garching b. München, (2004).

[44] K. Lackner et al. *"An algorithm for the solution of impurity diffusion under finite reaction rates."* Zeitschrift für Naturforschung, Vol.37a, No.5, p.931 (1982).

[45] G.M.D. Hogeweij. *"Degraded confinement and turbulence in tokamak experiments."* Fusion Sci. Technol., Vol.49, No.2T, p.277 (2006).

[46] K.-D. Zastrow et al. *"Helium exhaust experiments on JET with Type I ELMs in H-mode and with Type III ELMs in ITB discharges."* Nucl. Fusion, Vol.45, No.3, p.163 (2005).

[47] J.T. Hogan and D.L. Hillis. *"Helium transport and exhaust in tokamaks."* Nucl. Fusion, Vol.36, No.8, p.1079 (1996).

[48] E. Rebhan and G. van Oost. *"Thermonuclear burn criteria for D-T plasmas."* Fusion Sci. Technol., Vol 49, No.2T, p.16 (2006).

[49] A.J.H. Donné et al. *"Progress in the ITER Physics Basis: Diagnostics."* Nucl. Fusion, Vol.47, No.6, p.S337.

[50] O. Schmitz et al. *"Application of advanced edge diagnostics for transport studies in the stochastic boundary of TEXTOR-DED."* Invited lecture at PLASMA 2007 Greifswald, to be published in AIP Conference proceedings.

[51] E.J. Doyle et al. *"Progress in the ITER Physics Basis: Plasma confinement and transport."* Nucl. Fusion, Vol.47, No.6, p.S18.

[52] H.K. Park et al. *"Observation of high-field-side crash and heat transfer during sawtooth oscillation in magnetically confined plasmas."* Phys. Rev. Lett., Vol.96, 195003 (2007).

[53] K.H. Finken et al. *"Resonant coupling of ion-cyclotron waves to energetic helium ions."* Phys. Rev. Lett. Vol.73, No.3, p.436 (1994).

[54] D.S. Gray et al. *"Plasma exhaust and density control in tokamak fusion experiments with neutral beam or IRCF auxiliary heating."* Nucl. Fusion, Vol.38, No.11, p.1585 (1998).

[55] F.P. Orsitto et al. *"Requirements on fast particle measurements on ITER and candidate measurement techniques."* Nucl. Fusion, Vol.47, No.9, p.1311 (2007).